

604498

UNIVERSITY OF MINNESOTA  
INSTITUTE OF TECHNOLOGY

DEPARTMENT OF AERONAUTICAL ENGINEERING

Progress Report No 20

THEORETICAL PARACHUTE INVESTIGATIONS

Aeronautical Systems Division Contract No.

AF 33(616)-8310; Project No 6065; Task No 60252

1 December 1961 to 28 February 1962

Department of Aeronautics and Engineering  
Mechanics, No 5007?

University of Minnesota



MINNEAPOLIS 14, MINNESOTA

CLEARINGHOUSE FOR FEDERAL SCIENTIFIC AND TECHNICAL INFORMATION, CFSTI  
DOCUMENT MANAGEMENT BR 410.11

LIMITATIONS IN REPRODUCTION QUALITY

Accession #

604 498

- ☒ 1. We regret that legibility of this document is in part unsatisfactory. Reproduction has been made from best available copy.
- ☐ 2. A portion of the original document contains fine detail which may make reading of photocopy difficult.
- ☐ 3. The original document contains color, but distribution copies are available in black-and-white reproduction only.
- ☐ 4. The initial distribution copies contain color which will be shown in black-and-white when it is necessary to reprint.
- ☐ 5. Limited supply on hand; when exhausted, document will be available in Microfiche only.
- ☐ 6. Limited supply on hand; when exhausted document will not be available.
- ☐ 7. Document is available in Microfiche only.
- ☐ 8. Document available on loan from CFSTI (TT documents only).
- ☐ 9.

Processor:

*BL*

604498

COPY	1	OF	1	101
HARD COPY	\$ . 4.00			
MICROFICHE	\$ . 0.75			

101

Progress Report No 20 ✓  
THEORETICAL PARACHUTE INVESTIGATIONS

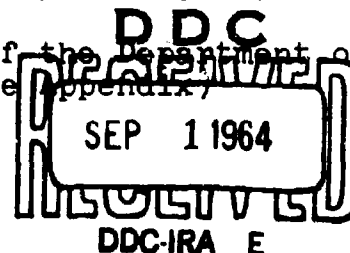
Aeronautical Systems Division Contract No.  
AF 33(616)-8310; Project No 6065; Task No 60252

1 December 1961 to 28 February 1962

Department of Aeronautics and Engineering  
Mechanics, No 5007

University of Minnesota

604498  
Dr. H. G. Heinrich, Professor, Department of Aeronautics and Engineering Mechanics  
Dr. T. Riabokin, Research Associate, Department of Aeronautics and Engineering Mechanics  
Prof. S. K. Ibrahim, Research Fellow, Department of Aeronautics and Engineering Mechanics  
Mr. E. L. Haak, Senior Engineer, Department of Aeronautics and Engineering Mechanics  
Mr. R. J. Niccum, Senior Engineer, Department of Aeronautics and Engineering Mechanics  
and graduate and undergraduate students of the Department of Aeronautics and Engineering Mechanics (see appendix)



62-05-5013

## TABLE OF CONTENTS

<u>Project No</u>		<u>Page</u>
1	Investigation of Wake Effects on the Behavior of Parachutes and Other Retardation Devices Behind Large Bodies at Subsonic and Supersonic Speeds . . . . .	2
	a) Width of Wake Behind Basic Bodies of Revolution in Subsonic Flow	
	b) Analytical Analysis of Turbulent Wake in Supersonic Flow	
4	Investigation of Basic Stability Parameters of Conventional Parachutes . . . . .	20
	a) Experimental Determination of the Apparent Moment of Inertia of Parachute Canopy Shapes	
	b) Wind Tunnel Investigation of Parachute Models	
7	Theoretical Study of Supersonic Parachute Phenomena . . . . .	29
	a) Supersonic Wind Tunnel Studies of Flexible Spiked Parachute	
	b) Pressure Distribution Studies on Spiked Parachute in Supersonic Flow	
	c) Supersonic Wind Tunnel Studies of Spiked Ribbon Parachutes	
8	Theoretical Analysis of the Dynamics of the Opening Parachute . . . . .	42
	a) Analytical Investigation of Parachute Inflation Time and Opening Force	
	b) Size-Force History of an Inflating Parachute	
	c) Drag Studies on Reefed Parachutes	
9	Statistical Analysis of Extraction Time, Deployment Time, Opening Time, and Drag Coefficient for Aerial Delivery Parachutes and Systems . . . . .	43

<u>Project No</u>		<u>Page</u>
10	Study of Basic Principles of New Parachutes and Retardation Devices . . . . .	44
12	Gliding Aerodynamic Decelerator . . . . .	45
13	Effective Porosity Studies . . . . .	54
	a) Parachute Cloths	
	b) Ribbon Grid Configurations	
14	Study of Flow Patterns of Aerodynamic Decelerators by Means of the Surface Wave Analogy . . . . .	62
	a) Stationary Model Water Channel	
16	Stress Analysis of the T-10 Troop Parachute . . . . .	71

# THEORETICAL PARACHUTE INVESTIGATIONS

## Progress Report No 20

### INTRODUCTION

1.0 This is the twentieth quarterly report covering the time from 1 December 1961 to 28 February 1962 on the study program on basic information of Aerodynamic Deceleration.

1.1 As in preceding reporting periods, work during this reporting period has been pursued in accordance with the technical program, and is described in the following sections of this report.

## Project No 1

### 2.0      Investigation of Wake Effects on the Behavior of Parachutes and Other Retardation Devices Behind Large Bodies at Subsonic and Supersonic Speeds.

#### 2.1      Width of Wake Behind Basic Bodies of Revolution in Subsonic Flow

##### 2.1.1      Introduction

In Ref 1, the velocity and pressure distribution in the wake and the width of the wake behind a fairly streamlined body of revolution were investigated. It was shown that the agreement between analytical predictions and measured results varied with the location of the investigated area, which led to the conclusion that the  $\mathcal{R}$  value should be considered as a function of the distance. A further extension of these studies was the investigation of the wakes of bodies with widely varying drag coefficients, with the general objective to establish the relationship between  $\mathcal{R}$  and the related drag coefficients as well as the variation of  $\mathcal{R}$  with the downstream distance.

The present effort in this field is the establishment of the width of the wake as a function of  $X/D$  using the experimental data presented in Progress Report No 17. It was postulated that this functional dependence of wake width could be presented in the form

$$\frac{b}{R} = k \left( \frac{X}{D} \right)^n, \quad (1.1)$$

where       $b$  = radial width of wake  
             $R$  = radius of primary body =  $D/2$   
             $n, k$  = constants  
             $X$  = distance behind body.

Equation (1.1) has the form

$$\log y = \log k + n \log x,$$

which plots as a straight line on log-log coordinate paper, with the slope  $n$  and intercept  $k$  easily determined.

### 2.1.2      Calculations

The experimental data for the models shown in Fig 1-1 was presented in Progress Report No 17 as a pressure coefficient,  $C_p$ , versus  $X/D$ , from which the velocity ratio was extracted and is presented in Figs 1-2 through 1-11 of this report. The experimental width of the wake was then defined as that point where the velocity defect is 10 percent of the velocity defect at the centerline; i.e.,  $(V_\infty - V_p)/(V_\infty - V_{CL}) = 0.10$ . Table 1-1 shows the numerical values and Fig 1-12 is a graphical presentation of the wake width so determined for the ten bodies.

It can be seen that the experimental data are merely approximately distributed along a straight line, which had to be expected. However, if one assumes straight lines for each curve of Fig 1-12, one obtains an approximate representation of wake width for all models over the  $X/D$  range from 2 to 20. This has been done, and the constants  $k$  and  $n$  so determined are presented in Table 1-2. Using these constants, the empirical wake width was calculated, and is presented in Figs 1-2 through 1-11, together with the velocity distributions, on the upper half of each graph. It should be noted that these graphs are scaled to be geometrically accurate.

In problems of aerodynamic retardation, the region from  $X/D = 3$  to  $X/D = 8$  is of particular interest. Therefore, the constants of the empirical wake width have been recalculated in an attempt to obtain a better agreement with experiment in this region. The constants  $k$  and  $n$  so determined are also presented in Table 1-2, and this empirical wake width is superimposed on the lower half of Figs 1-2 through 1-11. We see that quite accurate representations



are obtained. A further exploitation of these findings will be attempted during the next reporting period.

## 2.2 Analytical Analysis of Turbulent Wake in Supersonic Flow

### 2.2.1 Introduction

A set of linearized partial differential equations describing the velocity, pressure, temperature, and density fields in the wake of an axially symmetric body was derived and presented in Eqns (1.1c), (1.2c), (1.2d), and (1.6c) of Progress Report No 19. An error in printing was made in Eqn (1.2c). The first term on the right hand side should be

$$- (P_\infty / \rho_\infty U_\infty^2) \partial P^* / \partial x^*.$$

During this reporting period, an attempt was made to solve this set of equations. The results are presented in the following paragraphs. Symbols are as defined in Progress Report No 19.

### 2.2.2 Assumptions

To solve the set of linear differential equations, several assumptions must be made as follows:

- 1) The pressure, temperature, and density gradients in the axial direction are negligible

$$\left( \frac{\partial P^*}{\partial x^*} - \frac{\partial \rho^*}{\partial x^*} - \frac{\partial T^*}{\partial x^*} \approx 0 \right)$$

- 2) The shear stress in the radial direction is negligible ( $\tau_{xrt} \approx 0$ )
- 3) The shear stress in the axial direction is given by

$$\tau_{rx_T} = B_0 U_\infty^2 f(x^*) u_{\max}^* \frac{\partial u^*}{\partial r^*}, \quad (1.2)$$

where  $B$  = experimental constant  
 $f(x^*)$  = arbitrary function of  $x^*$  representing variation of turbulent viscosity in axial direction (to be determined experimentally)  
 $u_{\max}^*$  = maximum velocity defect (at  $r^* = 0$ ).

The first two assumptions are usually made in wake analysis, and should be very accurate at large distances downstream. It is difficult to justify the third assumption, since little is known about the turbulent shear stress in supersonic wakes. However, a similar form of the expression is widely used in incompressible wake analysis, with  $f(x^*)$  representing the local width of the wake. Therefore, it is hoped that Eqn (1.2) can be successfully employed in supersonic wake analysis.

Using these assumptions, the set of differential equations becomes:

Continuity:

$$\frac{\partial u^*}{\partial x^*} + \frac{1}{r^*} \frac{\partial}{\partial r^*} (r^* v^*) = 0, \quad (1.3)$$

x-momentum:

$$\frac{\partial u^*}{\partial r^*} = \frac{Bf(x^*)}{r^*} u_{\max}^* \frac{\partial}{\partial r^*} (r^* \frac{\partial u^*}{\partial r^*}), \quad (1.4)$$

r-momentum:

$$\frac{\partial v^*}{\partial x^*} = - \frac{P_{\infty}}{\rho_{\infty} U_{\infty}^2} \frac{\partial P^*}{\partial r^*}, \quad (1.5)$$

energy:

$$\frac{\partial T^*}{\partial x^*} = \frac{K}{r^* d\rho_{\infty} U_{\infty} C_v} \frac{\partial}{\partial r^*} \left( r^* \frac{\partial T^*}{\partial r^*} \right). \quad (1.6)$$

### 2.2.3

Solution for  $u^*$

To solve Eqn (1.4), we assume a solution of the form

$$u^* = g(x^*) e^{-h(x^*) r^{*2}} \quad (1.7)$$

We then obtain the term

$$\frac{1}{r^*} \frac{\partial}{\partial r^*} \left( r^* \frac{\partial u^*}{\partial r^*} \right) = 4g(x^*)h(x^*)e^{-h(x^*)r^{*2}} [r^{*2}h(x^*) - 1]. \quad (1.8)$$

Also, since  $u_{\max}^*$  occurs at  $r^* = 0$ , we have

$$u_{\max}^* = g(x^*). \quad (1.9)$$

Introducing Eqns (1.7), (1.8), and (1.9) into Eqn (1.4), we obtain

$$g'(x^*) + 4Bg^2(x^*)h(x^*)f(x^*) = [g(x^*)h'(x^*) + 4Bg^2(x^*)h^2(x^*)f(x^*)]r^{*2}, \quad (1.10)$$

where  $()'$  indicates differentiation with respect to  $x^*$ .

For this equation to be satisfied for all  $r^*$ , each side must be identically zero. Then we have

$$g'(x^*) + 4Bg^2(x^*)h(x^*)f(x^*) = 0, \quad (1.11)$$

$$g(x^*)h'(x^*) + 4Bg^2(x^*)h^2(x^*)f(x^*) = 0. \quad (1.12)$$

Multiplying Eqn (1.11) by  $h(x^*)$  and subtracting Eqn (1.12) from the result yields

$$g'(x^*)h(x^*) - g(x^*)h'(x^*) = 0, \quad (1.13)$$

which can be integrated to give

$$g(x^*) = K_1 h(x^*), \quad (1.14)$$

where  $K_1$  is a constant of integration. Substituting this

expression into Eqn (1.11) gives

$$\frac{dh(x^*)}{dx^*} = -4BK_1 f(x^*) h^3(x^*), \quad (1.15)$$

which can be integrated to give

$$h(x^*) = \left[ 8BK_1 \int f(x^*) dx^* + K_2 \right]^{-\frac{1}{2}}, \quad (1.16)$$

where  $K_2$  is a constant of integration.

Equation (1.7) now becomes

$$u^* = K_1 h(x^*) e^{-h(x^*) r^{*2}}, \quad (1.17)$$

where  $h(x^*)$  is given by Eqn (1.16).

#### 2.2.4 Solution for $v^*$

Subtracting Eqn (1.2) from Eqn (1.4) gives

$$\frac{Bf(x^*)}{r^*} u_{\max}^* \frac{\partial}{\partial r^*} \left( r^* \frac{\partial u^*}{\partial r^*} \right) = -\frac{1}{r^*} \frac{\partial}{\partial r^*} (r^* v^*), \quad (1.18)$$

which can be rewritten as

$$\frac{\partial}{\partial r^*} \left[ Bf(x^*) u_{\max}^* r^* \frac{\partial u^*}{\partial r^*} + r^* v^* \right] = 0, \quad (1.19)$$

or, after integration

$$v^* = -Bf(x^*) u_{\max}^* \frac{\partial u^*}{\partial r^*}. \quad (1.20)$$

Substituting the expression for  $u^*$  from Eqn (1.17) gives

$$v^* = 2BK_1^2 f(x^*) h^3(x^*) r^* e^{-h(x^*) r^{*2}}. \quad (1.21)$$

### 2.2.5 Solution for $p^*$

Substituting the value of  $\frac{\partial v^*}{\partial x^*}$  obtained from Eqn (1.21) into Eqn (1.5) yields

$$\frac{\partial p^*}{\partial r^*} = - \frac{\rho_{\infty} U_{\infty}^2}{p_{\infty}} 2BK_1^2 e^{-h(x^*)r^{*2}} r^* \left[ 3f(x^*)h^2(x^*)h'(x^*) + \right. \\ \left. + h^3(x^*)f'(x^*) - f(x^*)h^3(x^*)h'(x^*)r^{*2} \right]. \quad (1.22)$$

Integration and rearranging gives

$$p^* = \frac{BK_1^2 \rho_{\infty} U_{\infty}^2 h(x^*)}{p_{\infty}} \left[ 3f(x^*)h'(x^*) + f'(x^*)h(x^*) \right] e^{-h(x^*)r^{*2}} - \\ - \frac{BK_1^2 \rho_{\infty} U_{\infty}^2}{p_{\infty}} f(x^*)h(x^*)h'(x^*) \left[ h(x^*)r^{*2} + 1 \right] e^{-h(x^*)r^{*2}} + \\ + c(x^*), \quad (1.23)$$

where  $c(x^*)$  is an arbitrary function of  $x^*$ . To determine this function, use the fact

$$\lim_{r^* \rightarrow \infty} p^* = 0. \quad (1.24)$$

From Eqn (1.23) we see that

$$\lim_{r^* \rightarrow \infty} p^* = c(x^*). \quad (1.25)$$

Therefore  $c(x^*) = 0$ . Then Eqn (1.23) becomes

$$p^* = \frac{4B^2 K_1^3 \rho_{\infty} U_{\infty}^2 h^4(x^*) f^2(x^*)}{p_{\infty}} e^{-h(x^*)r^{*2}} \left[ h(x^*)r^{*2} + \right. \\ \left. + \frac{f'(x^*)}{4BK_1 h^2(x^*) f^2(x^*)} - 2 \right]. \quad (1.26)$$

### 2.2.6 Solution for $T^*$

Introduce the Prandtl and Reynolds numbers which are defined respectively as

$$P_r = \frac{c_p \mu}{K}, \quad Re = \frac{\rho_\infty U_\infty d}{\mu}, \quad (1.27)$$

where  $c_p$  = specific heat of fluid at constant pressure  
 $d$  = characteristic dimension of body  
 $K$  = thermal conductivity of fluid  
 $U_\infty$  = free stream velocity  
 $\mu$  = dynamic viscosity of fluid.

Then Eqn (1.6) becomes

$$\frac{RePr}{\gamma} \frac{\partial T^*}{\partial x^*} = \frac{\partial^2 T^*}{\partial r^{*2}} + \frac{1}{r^*} \frac{\partial T^*}{\partial r^*}. \quad (1.28)$$

We assume a solution of the form

$$T^* = g_1(x^*) e^{-h_1(x^*) r^{*2}}. \quad (1.29)$$

Then Eqn (1.28) becomes

$$\left[ \frac{RePr}{\gamma} \frac{g_1'(x^*)}{g_1(x^*)} + 4h_1(x^*) \right] = r^{*2} \left[ \frac{RePr}{\gamma} h_1'(x^*) + 4h_1^2(x^*) \right]. \quad (1.30)$$

Since this must be satisfied for all  $r^*$ , both sides of the equation must be identically zero. Then

$$\frac{RePr}{\gamma} \frac{g_1'(x^*)}{g_1(x^*)} + 4h_1(x^*) = 0 \quad (1.31)$$

$$\frac{RePr}{\gamma} h_1'(x^*) + 4h_1^2(x^*) = 0. \quad (1.32)$$

Solving Eqn (1.32) for  $h_1(x^*)$  gives

$$h_1(x^*) = \left[ \frac{4\gamma x^*}{RePr} + K_3 \right]^{-1}, \quad (1.33)$$

where  $K_3$  is a constant of integration. Substituting this expression into Eqn (1.31) and solving for  $g_1(x^*)$  yields

$$g_1(x^*) = K_4 \left[ \frac{4\gamma x^*}{RePr} + K_3 \right]^{-1} = K_4 h_1(x^*), \quad (1.34)$$

where  $K_4$  is a constant of integration.

Substituting Eqns (1.33) and (1.34) into Eqn (1.29) yields the expression for the temperature field

$$T^* = K_4 h_1(x^*) e^{-h_1(x^*) r^{*2}}, \quad (1.35)$$

where  $h_1(x^*)$  is given by Eqn (1.33).

## 2.2.7 Summary

The equations describing the flow field have been derived and are:

$$u^* = K_1 h(x^*) e^{-h(x^*) r^{*2}}, \quad (1.17)$$

$$v^* = 2BK_1^2 f(x^*) h^3(x^*) r^* e^{-h(x^*) r^{*2}}, \quad (1.21)$$

$$p^* = 4B^2 K_1^3 \gamma h^4(x^*) f^2(x^*) \left[ h(x^*) r^{*2} + \frac{f'(x^*)}{4BK_1 h^2(x^*) f^2(x^*)} - 2 \right] e^{-h(x^*) r^{*2}}, \quad (1.26)$$

$$T^* = K_4 h_1(x^*) e^{-h_1(x^*) r^{*2}}, \quad (1.35)$$

$$\text{Where } h(x^*) = \left[ 8BK_1 \int f(x^*) dx^* + K_2 \right]^{-\frac{1}{2}}, \quad (1.16)$$

$$h_1(x^*) = \left[ \frac{4\gamma x^*}{RePr} + K_3 \right]^{-1} \quad (1.33)$$

and  $K_1$ ,  $K_2$ ,  $K_3$ , and  $K_4$  are constants of integration to be determined by experiment.

### 2.2.8      Proposed Work











During the next reporting period, a comparison will be initiated between the above theory and experiments, and the constants of integration will be determined for various bodies.

### REFERENCES











1.    Heinrich, H. G. and Riabokin, T.: Analytical and Experimental Considerations of the Velocity Distribution in the Wake of a Body of Revolution, WADC TR 60-257, December 1959.
2.    Schlichting, H.: Boundary Layer Theory, McGraw-Hill, New York, 1955.

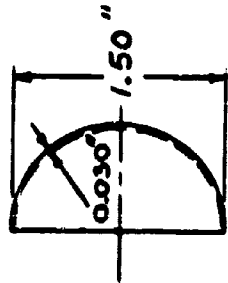


# TABLE 1-1. EXPERIMENTAL WAKE WIDTH

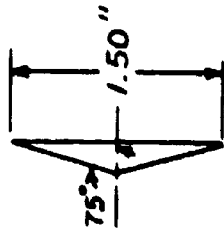
MODEL		$\frac{x}{D} = 2$	$\frac{x}{D} = 4$	$\frac{x}{D} = 6$	$\frac{x}{D} = 8$	$\frac{x}{D} = 10$	$\frac{x}{D} = 12$	$\frac{x}{D} = 16$	$\frac{x}{D} = 20$
A 	$\frac{b}{R}$	1.70	2.55	3.50	3.70	4.00	4.50	6.00	6.30
B 	$\frac{b}{R}$	1.75	2.25	2.55	2.90	3.40	4.00	4.50	5.00
C 	$\frac{b}{R}$	1.70	2.30	2.60	2.80	3.40	3.80	4.20	4.80
D 	$\frac{b}{R}$	1.70	2.15	2.50	2.80	3.10	3.80	4.60	5.00
E 	$\frac{b}{R}$	1.30	1.85	2.25	2.50	2.80	2.90	3.50	4.20
F 	$\frac{b}{R}$	1.35	1.75	2.25	2.25	2.70	2.90	2.90	3.40
G 	$\frac{b}{R}$	1.03	1.20	1.75	1.95	2.00	2.00	2.30	2.50
H 	$\frac{b}{R}$	0.80	0.98	1.65	1.55	1.75	1.85	2.40	2.80
I 	$\frac{b}{R}$	0.72	0.85	1.20	1.40	1.60	1.90	2.20	2.30
J 	$\frac{b}{R}$	0.82	0.90	1.50	1.75	1.70	1.70	2.20	2.50

# TABLE 1-2. EMPIRICAL WAKE WIDTH CONSTANTS

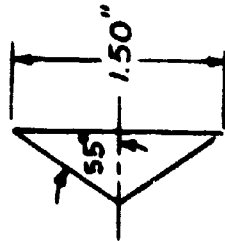
MODEL	$C_{D_0}$	$2 \leq x/D \leq 20$		$2 \leq x/D \leq 8$	
		k	n	k	n
A 	1.40	1.14	0.582	1.124	0.598
B 	1.03	1.33	0.394	1.369	0.353
C 	0.836	1.34	0.384	1.353	0.363
D 	0.743	1.32	0.393	1.340	0.361
E 	0.577	0.927	0.488	0.929	0.485
F 	0.425	0.985	0.397	0.966	0.440
G 	0.230	0.810	0.376	0.804	0.385
H 	0.206	0.541	0.522	0.522	0.562
I 	0.197	0.493	0.531	0.504	0.474
J 	0.194	0.565	0.491	0.571	0.488



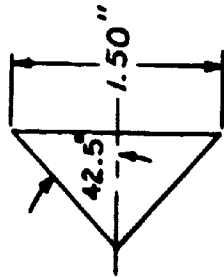
MODEL A  
HOLLOW HEMISPHERE  
(OPEN TO FLOW)  
 $C_D = 1.40$



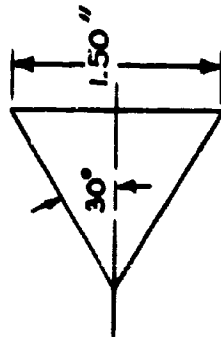
MODEL B  
CONE  
 $C_D = 1.03$



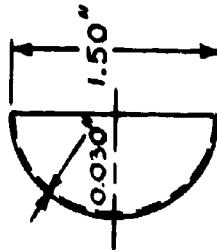
MODEL C  
CONE  
 $C_D = 0.836$



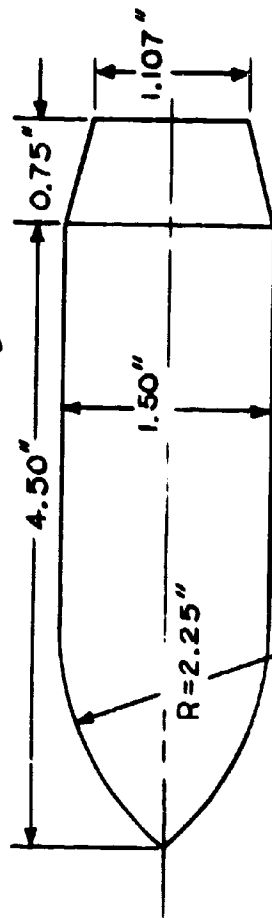
MODEL D  
CONE  
 $C_D = 0.743$



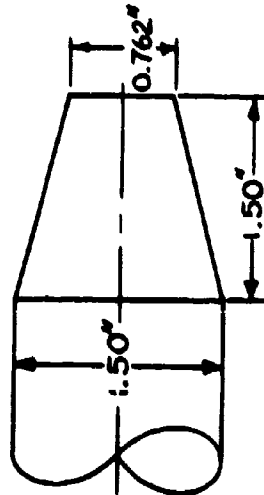
MODEL E  
CONE  
 $C_D = 0.577$



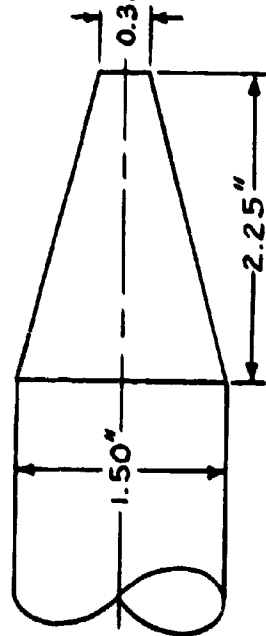
MODEL F  
HOLLOW HEMISPHERE  
(CLOSED TO FLOW)  
 $C_D = 0.425$



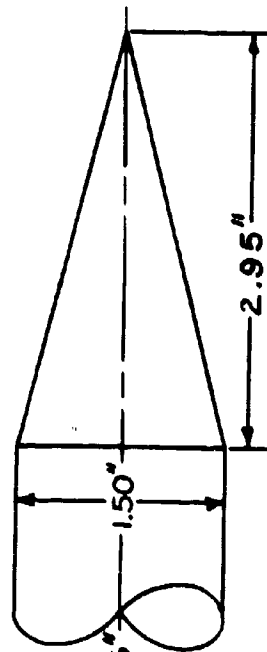
MODEL G  
OGIVE CYLINDER WITH  
AFTERBODY NO. 1.  
 $C_D = 0.230$



MODEL H  
OGIVE CYLINDER WITH  
AFTERBODY NO. 2.  
 $C_D = 0.206$



MODEL I  
OGIVE CYLINDER WITH  
AFTERBODY NO. 3.  
 $C_D = 0.197$



MODEL J  
OGIVE CYLINDER WITH  
AFTERBODY NO. 4.  
 $C_D = 0.194$

FIG 1-1. BODIES OF REVOLUTION

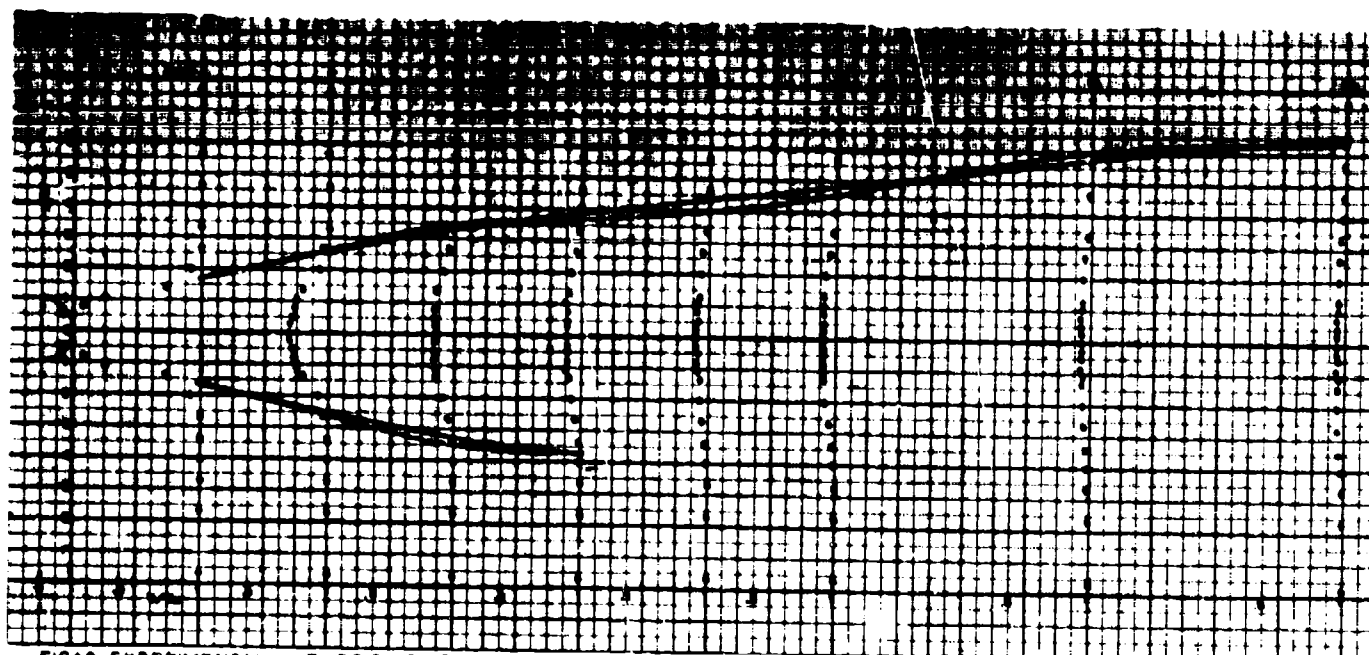


FIG12. EXPERIMENTAL VELOCITY DISTRIBUTION IN WAKE OF HOLLOW HEMISPHERE (CUP FORWARD)—MODEL A  
WAKE WIDTH: EXPERIMENTAL — — —  
EMPIRICAL ———

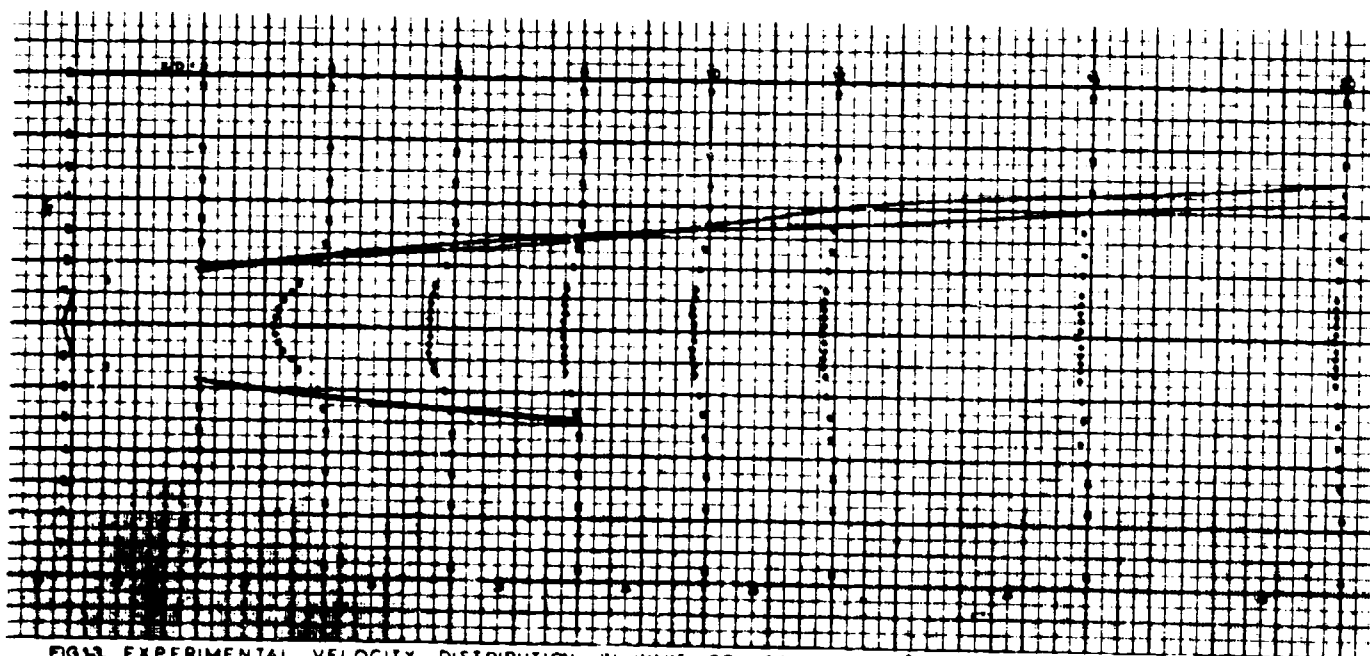


FIG13. EXPERIMENTAL VELOCITY DISTRIBUTION IN WAKE OF CONE ( $\alpha = 75^\circ$ )—MODEL B  
WAKE WIDTH: EXPERIMENTAL — — —  
EMPIRICAL ———

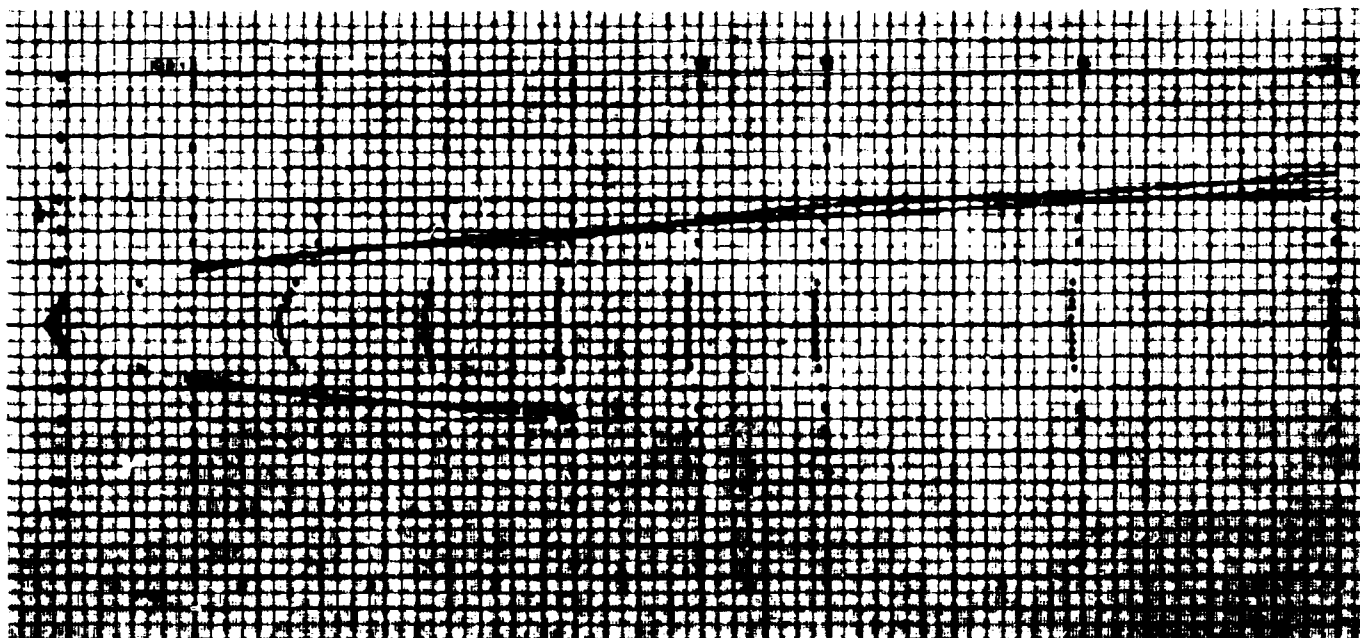


FIG. 4. EXPERIMENTAL VELOCITY DISTRIBUTION IN WAKE OF CONE ( $\alpha = 25^\circ$ ) - MODEL C  
 WAKE WIDTH: EXPERIMENTAL - - -  
 EMPIRICAL - - - -



FIG. 5. EXPERIMENTAL VELOCITY DISTRIBUTION IN WAKE OF CONE ( $\alpha = 42.5^\circ$ ) - MODEL D  
 WAKE WIDTH: EXPERIMENTAL - - -  
 EMPIRICAL - - - -

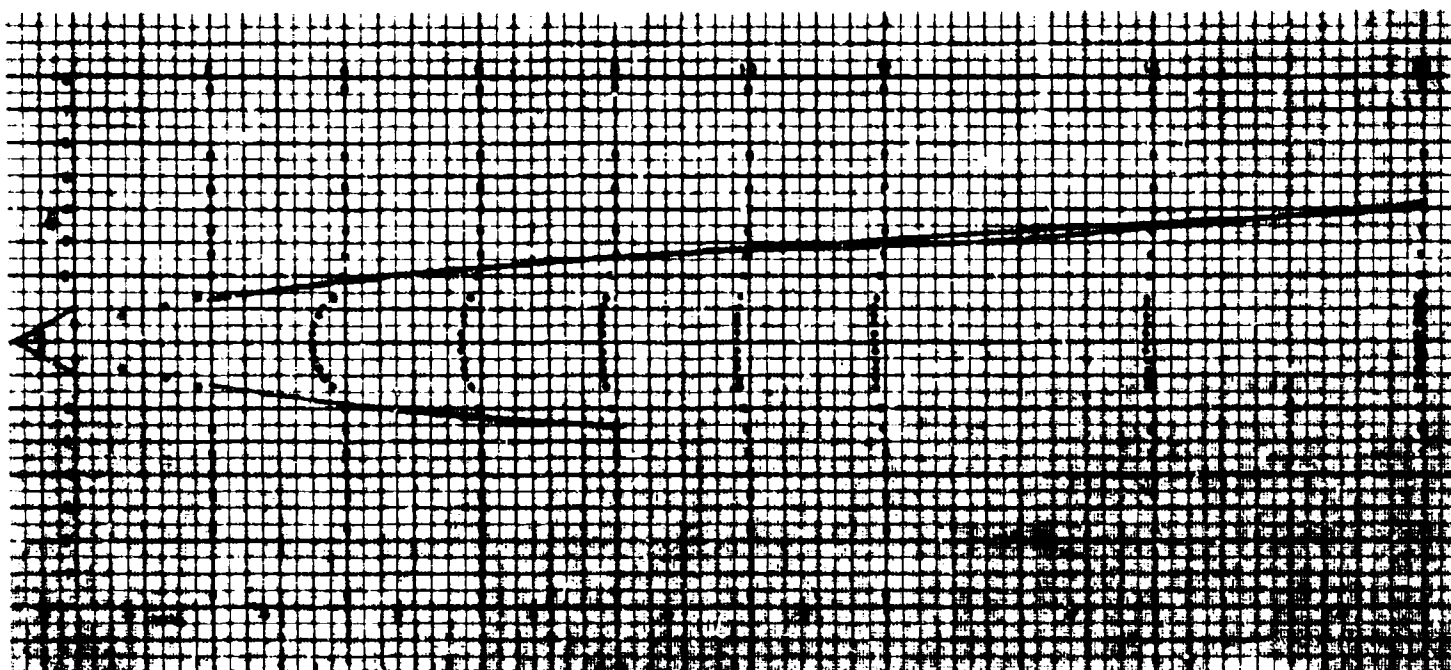


FIG16. EXPERIMENTAL VELOCITY DISTRIBUTION IN WAKE OF CONE ( $\alpha = 30^\circ$ )—MODEL E  
WAKE WIDTH: EXPERIMENTAL ---  
EMPIRICAL ———

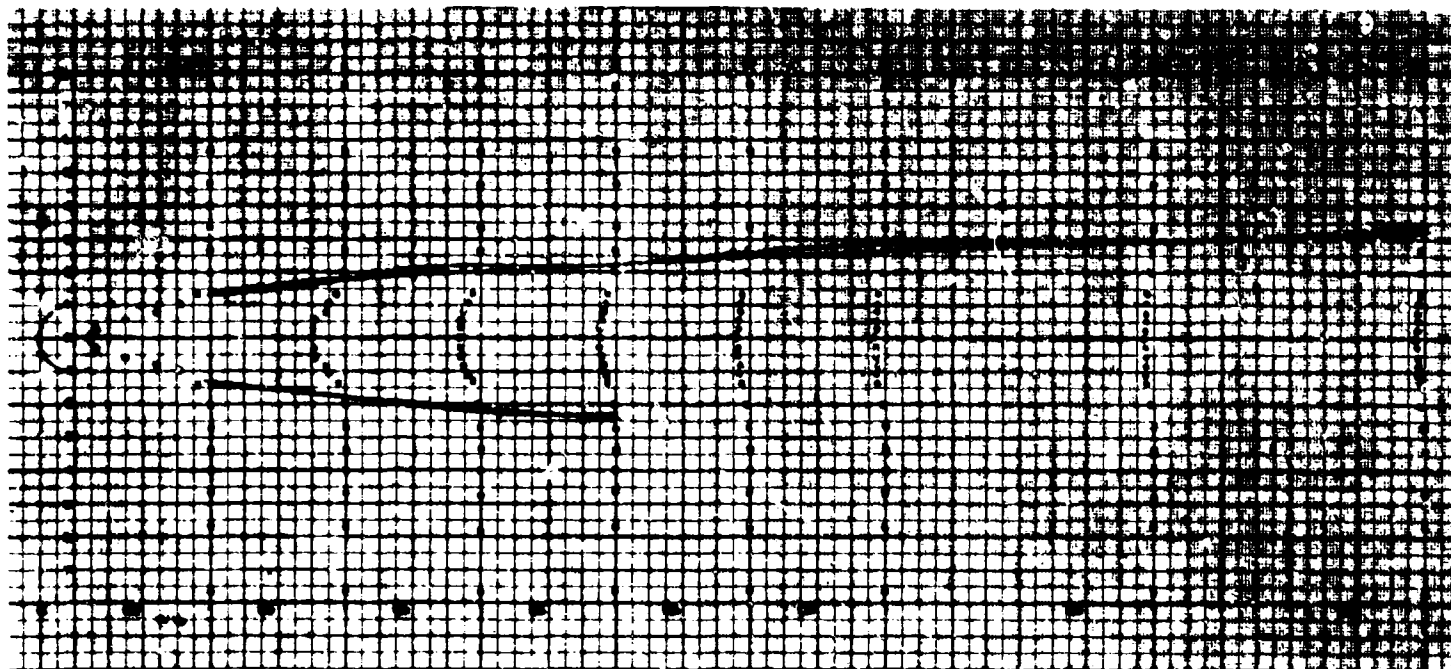


FIG17. EXPERIMENTAL VELOCITY DISTRIBUTION IN WAKE OF HOLLOW HEMISPHERE (CUP BACKWARD)—MODEL F  
WAKE WIDTH: EXPERIMENTAL ---  
EMPIRICAL ———

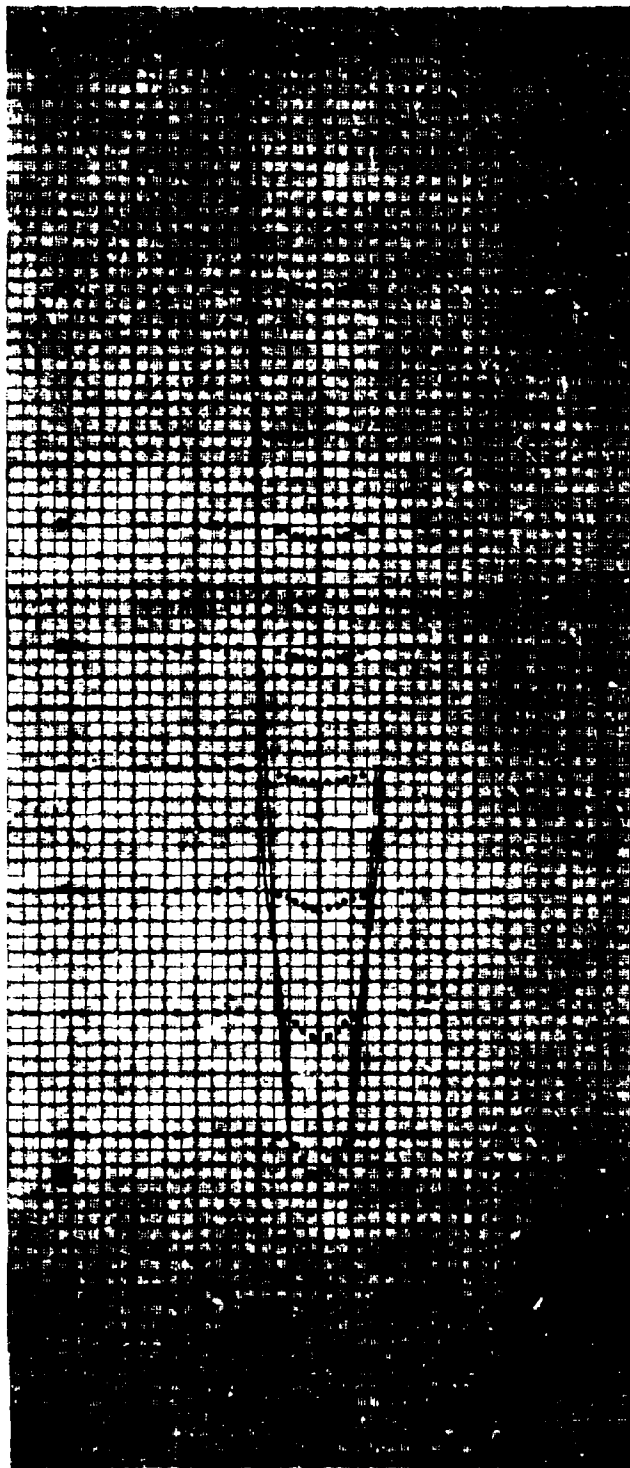


FIG. 8. EXPERIMENTAL VELOCITY DISTRIBUTION IN WAKE OF OGIVE CYLINDER WITH AFTERBODY NO. 1—MODEL G  
WAKE WIDTH: EXPERIMENTAL — — —  
WAKE WIDTH: EMPIRICAL —

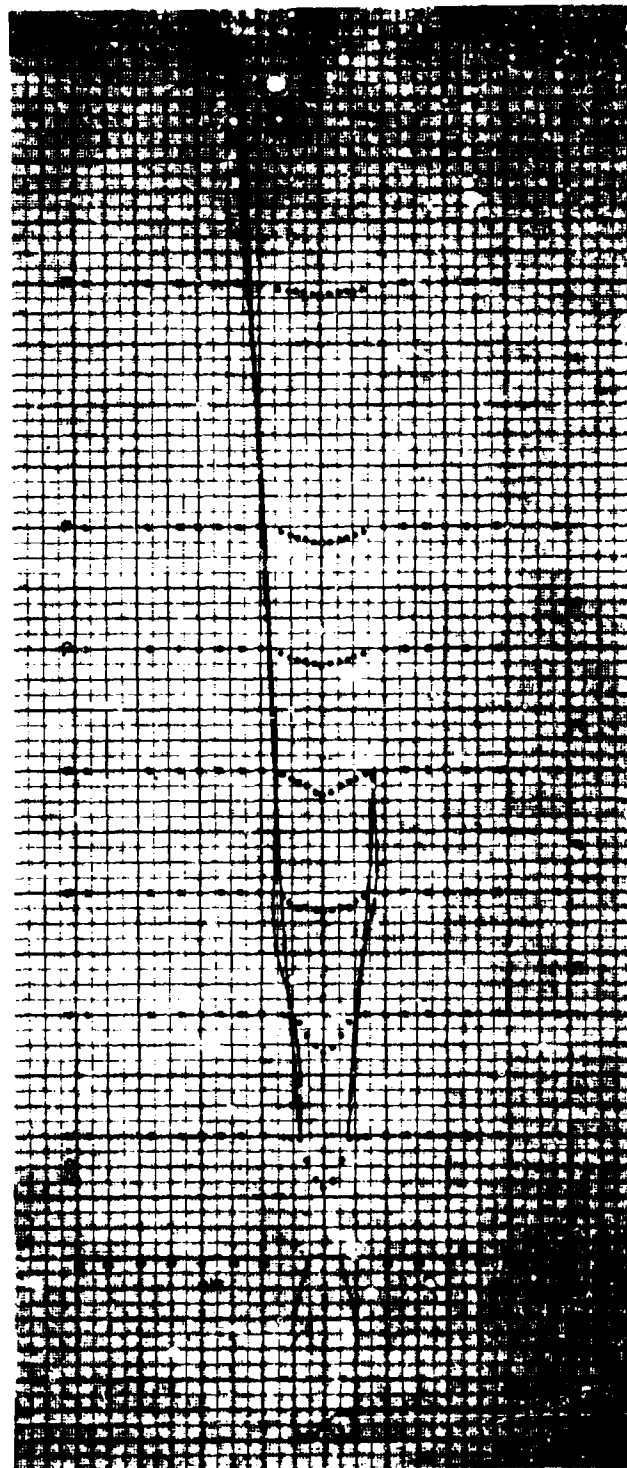


FIG. 10. EXPERIMENTAL VELOCITY DISTRIBUTION IN WAKE OF OGIVE CYLINDER WITH AFTERBODY NO. 2—MODEL H  
WAKE WIDTH: EXPERIMENTAL — — —  
WAKE WIDTH: EMPIRICAL —

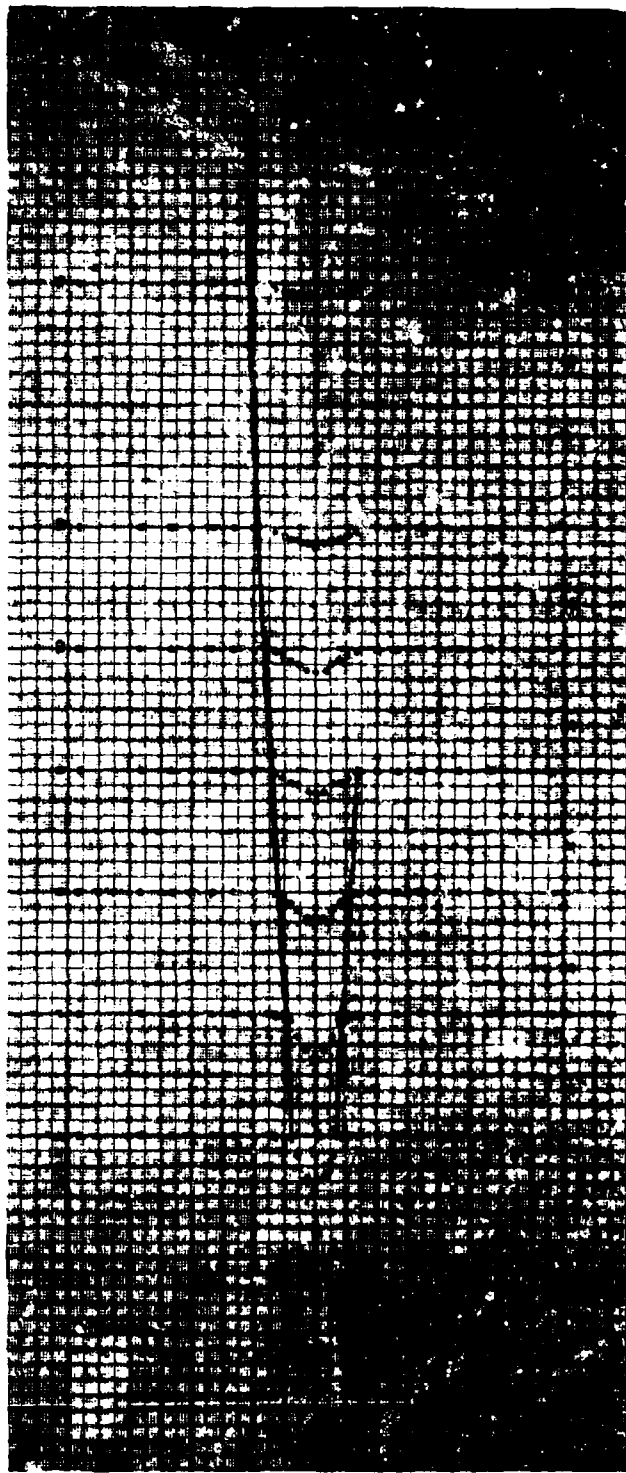


FIG. 10. EXPERIMENTAL VELOCITY DISTRIBUTION IN WAKE OF OGIVE CYLINDER WITH AFTERBODY NO. 3—MODEL 1  
WAKE WIDTH: EXPERIMENTAL ———  
WAKE WIDTH: EMPIRICAL ———

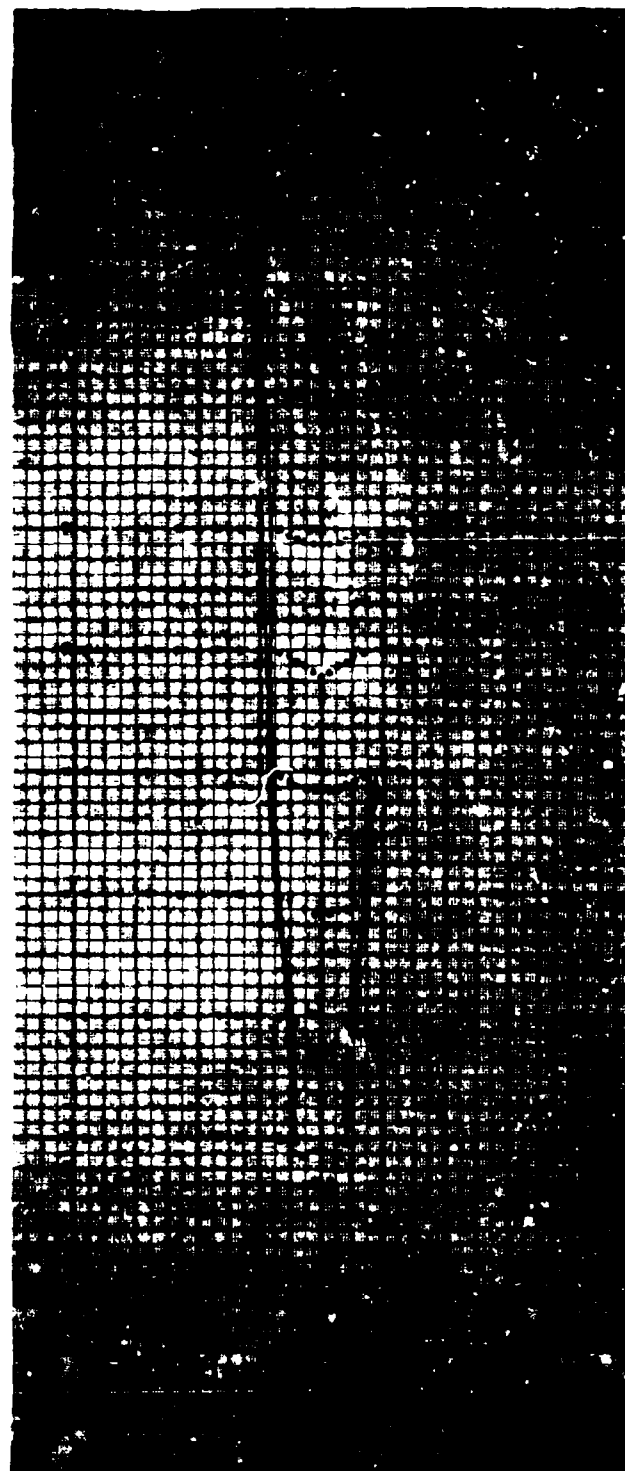


FIG. 11. EXPERIMENTAL VELOCITY DISTRIBUTION IN WAKE OF OGIVE CYLINDER WITH AFTERBODY NO. 4—MODEL 3  
WAKE WIDTH: EXPERIMENTAL ———  
WAKE WIDTH: EMPIRICAL ———

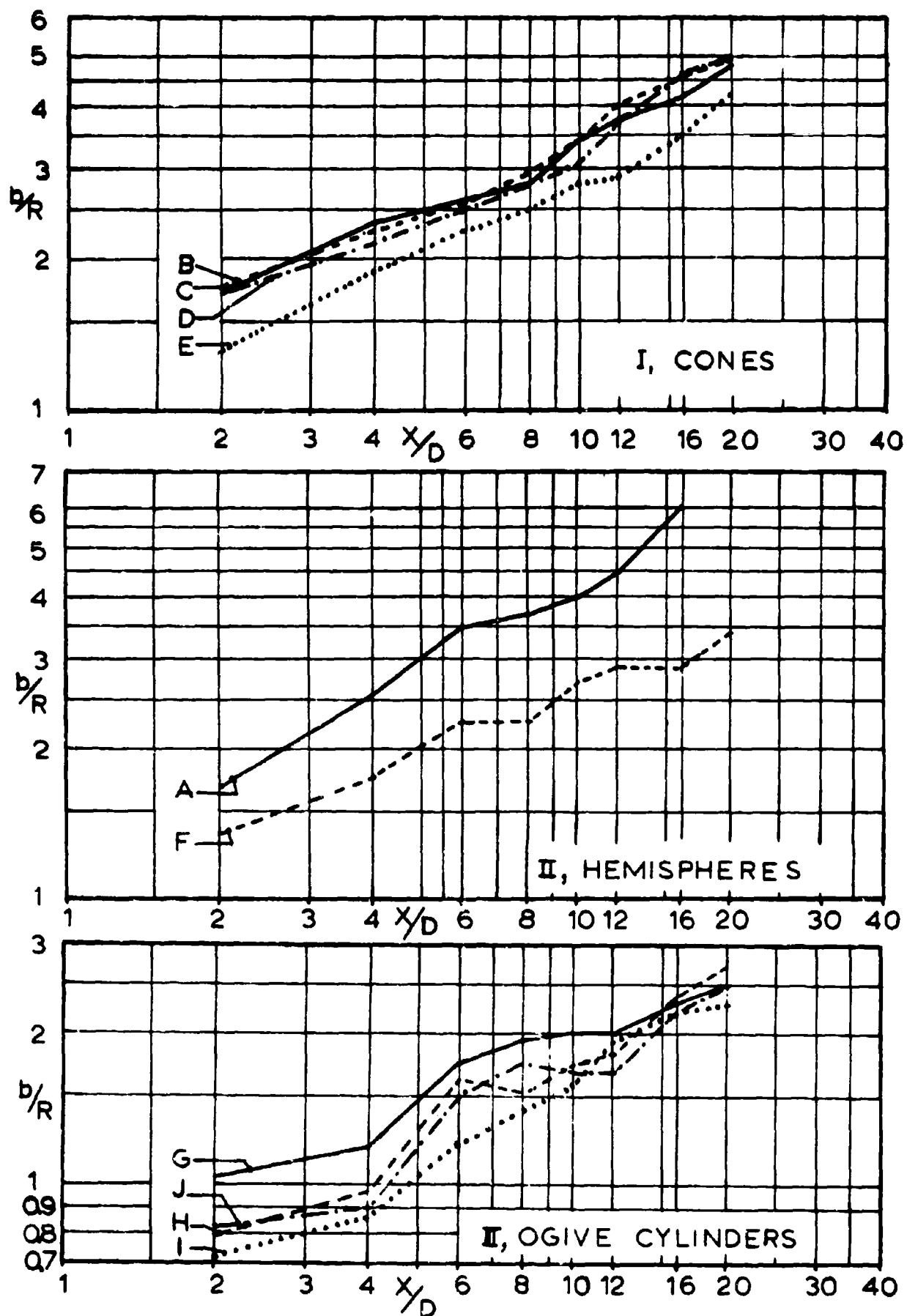


FIG1-12. EXPERIMENTAL WAKE WIDTH AS A FUNCTION OF  $X/D$



## Project No 4

### 3.0      Investigation of Basic Stability Parameters of Conventional Parachutes

#### 3.1      Experimental Determination of the Apparent Moment of Inertia of Parachutes

##### 3.1.1      Introduction

In setting up the dynamic stability equations for parachutes, it is necessary to consider the apparent mass and the apparent moment of inertia of the parachute.

Strictly speaking, the moment of inertia of a body applies only for motion in a vacuum. When the motion takes place in a fluid, the virtual or apparent moment of inertia must be considered in order to account for the inertia of the fluid mass affected by the motion. The added inertia will depend on the body shape and motion and the density of the fluid.

The analytical determination of the apparent mass and apparent moment of inertia is very difficult and the available theories can be applied only to simple geometrical shapes such as spheres and ellipsoids. For shapes of practical interest such as parachute canopies, it is necessary at present to resort to experimentation for determining the apparent mass and apparent moment of inertia.

##### 3.1.2      Literature Survey

In order to determine the best experimental method for measuring the apparent moment of inertia of parachute canopy shapes, an extensive literature survey was made. The following brief comments deal with the more relevant and significant references surveyed.

Reference 1 gave a detailed analytical treatment for the case of solid, symmetric bodies revolving in a fluid and presented values of the inertia coefficients "k" enabling the

calculation of the apparent additional masses and the apparent additional moments of inertia for various ellipsoids. The shapes analyzed are not of specific interest for parachute work, but the data presented may be of value for a comparison with experimentally obtained results or a check on experimental technique.

References 2 and 3 dealt with the experimental determination of the moments of inertia of airplanes and suggested a somewhat similar arrangement for rigid parachute models. Preliminary tests with this arrangement proved impractical as mentioned below. References 4 and 5 described methods for the experimental determination of the added mass and added mass moment of inertia of a ship model. It was found in Reference 5, for example, that the added mass and mass moment of inertia for heaving and pitching were of the same order of magnitude as those of the ship itself. It may be mentioned that while the motions of a ship model differ from those of a parachute, the underlying theory and experimental techniques have many features in common.

Reference 6 presented a simple experimental arrangement for determining the virtual mass and moments of inertia of discs and cylinders. In view of its relative simplicity and adaptability, it was decided to use a very similar experimental arrangement for our purpose; the underlying theory of the method is given below.

References 7 and 8 use the same basic principle to determine the added masses for lenses, parallel plates, spheres, and cubes. Reference 9 treats the problem of the virtual mass of two-dimensional shapes and gives a coordinated theoretical and experimental investigation of clusters of parallel circular cylinders. In a specific example given, the theory was confirmed to within an experimental error of  $\pm 6\%$ .

### 3.1.3      Experimental Arrangements

As indicated above, a simple experimental arrangement

suggested by References 2 and 3 was first tried. It consisted essentially of a bi-filar torsion pendulum to which is attached the model under test. By measuring the period of oscillation in air and in a vacuum and allowing for the characteristics of the suspension system, the apparent moment of inertia of the model under test could be calculated. However, preliminary tests with a hemispherical cup oscillating in still air and in the test section of the low density wind tunnel with no flow gave very little change in the period of oscillation. It was concluded that unfavorable experimental facts such as limited model size, unavoidable frictional losses in the suspension system, slight unsymmetries in the model and mounting, etc., made this particular arrangement impractical.

Another experimental arrangement based on that of Reference 6 was set up, and preliminary tests indicated its suitability. It consists of a specially designed test frame incorporating a simple torsion pendulum, adjustable mounting arms for the models and the necessary apparatus for sensing, recording, and timing the oscillations. Figure 4-1 illustrates the main dimensions and design features of the test frame. The torsion rod now used is 1/8 inch in diameter, 22 inches long, and is mounted vertically and held fixed at both ends. A small fitting is clamped on the rod at mid-point and carries two threaded 3/32 inch diameter shafts for mounting the models such that the torsional oscillation of the central rod imparts the model motion under investigation.

For symmetry, two identical models mounted on opposite arms are used unless the motion is about an axis of symmetry in which case a single model would be attached directly to the torsion shaft at mid-point. In other words, the center of gravity of the model system is made to coincide with that of the torsion rod. The dimensions of the test frame were chosen so that it can be conveniently immersed in a tank containing water or some other convenient liquid such as gasoline ( $\rho = 0.734 \text{ gm/cm}^3$ ).

A small, linear variable differential transformer (Shaevitz) is used as a transducer to pick up the oscillations. The coil is mounted in a plexiglass fitting attached to the top member of the test frame while the core is mounted on another plexiglass fitting attached to the crossarm fitted to the torsion rod near the top as shown. Means are provided for initially centering the core of the transducer. The transducer is mounted near the upper end of the torsion rod so that it is just above the immersion level.

Figure 4-2 is a photograph of the test frame showing the transducer and a pair of circular discs as models. Figure 4-3 illustrates in addition the amplifying, recording, and timing equipment used. This consists of a Brush Strain Analyser model BL-310, a two channel Brush pen recorder, a variable frequency oscillator, and a Cathode Ray oscilloscope.

So far the reservoir tank of the water analogy facility has been used for the tests in water.

#### 3.1.4 Theory

The period of oscillation of a stretched wire held at both ends as shown in Fig 4-1 and subjected to torsional oscillation is given by (Ref 6)

$$T = 2\pi \sqrt{\left( \frac{K}{I} - \frac{b^2}{4I^2} \right)^{-1}}, \quad (4.1)$$

where  $K$  = torsional constant of the wire  
 $I$  = effective moment of inertia of the cross arm  
 and parts attached to it  
 $b$  = damping factor due to the liquid.

The quantity  $b/2I$  can be determined experimentally for the liquid used. If the experimental parameters are arranged in such a way that  $b^2/4I^2$  is very much smaller than  $K/I$ , then the term  $b^2/4I^2$  may be neglected and Eqn (4.1) may be simplified to

$$T \approx 2\pi \sqrt{\frac{I}{K}}. \quad (4.2)$$

If tests for a given model arrangement are conducted in air and in a liquid, then

$$T_a \approx 2\pi \left( \frac{I_a}{K} \right)^{\frac{1}{2}} \quad (4.3)$$

and

$$T_l \approx 2\pi \left( \frac{I_l}{K} \right)^{\frac{1}{2}}. \quad (4.4)$$

The virtual moment of inertia of the entire oscillating member due to the liquid is given by:

$$I_l - I_a = \frac{K}{4\pi^2} (T_l^2 - T_a^2). \quad (4.5)$$

If the virtual moment of inertia of the system without the models attached is  $I_s$ , then the virtual moment of inertia of the model system alone will be given by

$$I_v = I_l - I_a - I_s = \frac{K}{4\pi^2} (T_l^2 - T_a^2) - I_s \quad (4.6)$$

In the case of a symmetric arrangement of two models as shown in Figure 4-1, the virtual moment of inertia of each model will be one half that given by Eqn (4.6).

Experimentally, therefore, it is only necessary to measure the period of oscillation of the whole system in air ( $T_a$ ), in liquid ( $T_l$ ), the period of oscillation of the system in liquid but without the models attached ( $T_s$ ), and the torsional constant of the cone  $K$ . The latter may be obtained by a separate experiment.

Since the virtual moment of inertia is directly proportional to the density of the liquid, the values obtained can be expressed for some other fluid of specified density.

### 3.1.5 Proposed Work

In the next reporting period, the experimental parameters

such as torsion constant and model size will first be optimized. Next, some standard body shapes will be tested and the experimental results obtained will be compared with the predictions of theoretical analysis and available experimental data.

When satisfactory agreement is achieved between theory and experiment, tests with rigid canopy models of the circular flat, ribbon, and ribless guide surface parachutes will be conducted.

It is also proposed to introduce certain modifications and refinements to the test apparatus and experimental techniques.

### 3.2 Wind Tunnel Investigation of Parachute Models

The final draft of the technical report entitled "Stability and Drag of Parachutes with Varying Effective Porosity" has been submitted to the Procuring Agency for approval.

Note: The effective porosity studies of common parachute cloths previously reported under this project are now presented together with effective porosity studies on ribbon and grid configurations under Project 13, "Effective Porosity Studies."

## REFERENCES

1. Zahm, A. P.: Flow and Force Equations for a Body Revolving in a Fluid, Parts IV and V, NACA TR 323, 1929.
2. Miller, M. P.: An Accurate Method of Measuring the Moments of Inertia of Airplanes, NACA TN 351.
3. Soule, H. A., and Miller, M. P.: The Experimental Determination of the Moments of Inertia of Airplanes, NACA TR 467, 1933.
4. Geritsma, I. J.: Experimental Determination of Damping, Added Mass and Added Mass Moment of Inertia of a Ship Model, International Shipbuilding Progress No 4, 1952, p. 505.
5. Vossers, I. G.: Fundamentals of the Behavior of Ships in Waves, Part II, Article 14, International Shipbuilding Progress, Volume 6, 1959, p. 538.
6. Yu, Yee Tak: Virtual Masses and Moments of Inertia of Discs and Cylinders in Various Liquids, Journal of Applied Physics, 1942, Volume 13, pp. 66-69.
7. Stelson, J. M., and Navid, F. T.: Virtual Mass and Acceleration in Fluids, Trans., ASCE, Volume 22, 1957, pp. 518-530.
8. Sarpkaya, Turgut: Added Mass of Lenses and Parallel Plates, Journal Eng. Mech. Div. ASCE, June, 1960.
9. Ashley, Holt, and Asher, Gifford W.: On the Virtual Mass of Clustered Boosters, MIT Fluid Dynamics, Res. Lab. Report No 60-7, December, 1960.

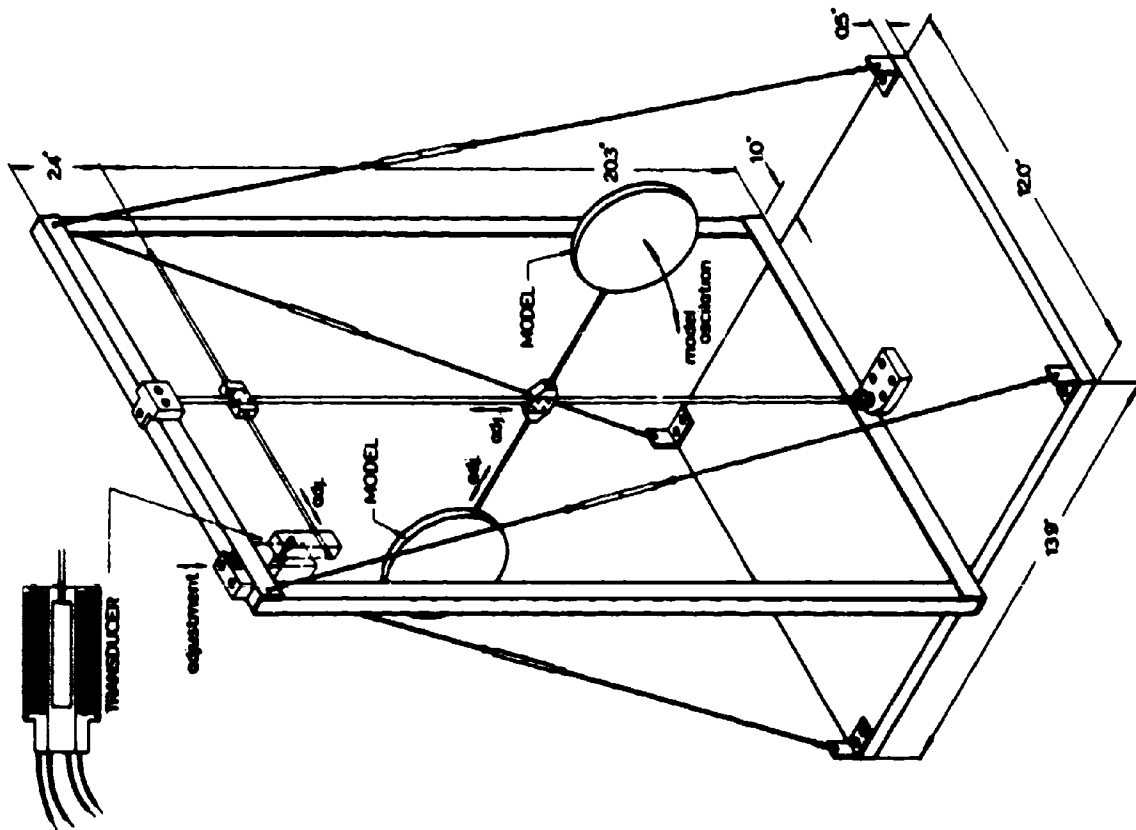


FIG 4-1. SKETCH OF TEST FRAME FOR THE EXPERIMENTAL DETERMINATION OF THE APPARENT MOMENT OF INERTIA

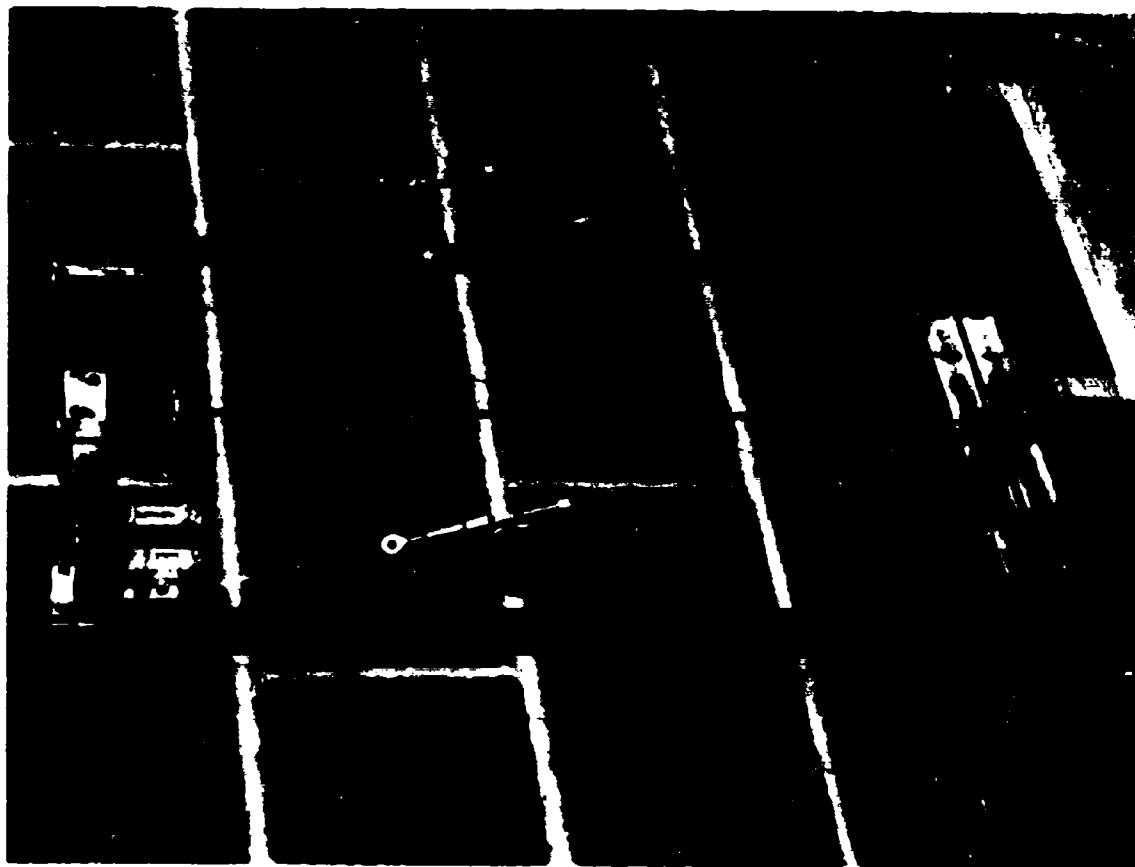


FIG 4-2. TEST FRAME WITH A PAIR OF CIRCULAR DISKS AS MODELS.





FIG 4-3. TEST FRAME AND SUPPORTING TEST EQUIPMENT.

## Project No 7

### 4.0      Theoretical Study of Supersonic Parachute Phenomena

#### 4.1      Introduction

This study has analyzed the behavior of conventional parachutes in supersonic flow in the wind tunnel and by means of the water analogy. Based on this analysis, a supersonic decelerator was conceived which utilizes a pressure reducing "spike " in connection with a solid cloth canopy.

Progress Reports Nos 18 and 19, Project No 10, presented results of initial attempts to use the same concept in a combination which includes a ribbon parachute canopy. Since this investigation is so closely connected to the study of the original form of the spiked parachute, it has been decided to present the two parallel investigations together under this project.

The work done during this reporting period will be reported in the following phases:

- a) Supersonic wind tunnel studies of flexible spiked parachutes
- b) Pressure distribution studies on spiked parachutes in supersonic flow
- c) Supersonic wind tunnel studies of spiked ribbon parachutes.

#### 4.2      Supersonic Wind Tunnel Studies of Flexible Spiked Parachute

##### 4.2.1      Past Work

Rigid models of the spiked parachute have been found stable in wind tunnel tests at Mach numbers of 1.14, 2.0, and 3.0, both with and without suspension lines. Progress Reports Nos 17, 18, and 19 reported results of tests on configurations with textile canopies.

In the early tests with flexible canopies, both the model and the tunnel suspension system suffered mechanical damage, prompting design of a new tunnel suspension system and a deployment device. These systems have proven satisfactory. Damage to the models was reduced through the use of heavier MIL-C-8021A, Type II nylon cloth (300 lb/in), elimination of wire rings in the canopy, and improvement of the suspension line connections.

#### 4.2.2 Continuation

Tests have been continued during the present reporting period on the spiked parachute with flexible canopy. During the early part of the period, models continued to suffer damage to their suspension system. However, it is felt that this problem has now been eliminated through the use of a cone cast from polystyrene foam, which is much lighter and more resilient than the materials previously used. As shown in Fig 7-1, the polystyrene foam is molded within a nylon cloth cone to which the suspension lines have been previously sewn. Using this modified cone and suspension system, fifteen tests have been made with nearly 75% of the models recovered undamaged.

The use of a lighter cone was also prompted by the fact that the canopy and cone tended to oscillate during testing as independent bodies in a two-mass system. Thus the lighter cone has solved this problem of dynamic balance while simultaneously reducing greatly the number of suspension line connection failures.

During this reporting period a new deployment method was used. As shown in Fig 7-2, the system includes a basket which holds the cone and the reefed canopy. After the flow in the tunnel is established, the basket is slipped off from the decelerator through a downstream movement.

Figure 7-3 presents sequences of Schlieren photographs taken at intervals from a test of a model with a polystyrene foam cone which was deployed as described above. As seen, the model

was fully inflated during the test run lasting 30 seconds. The maximum amplitude of oscillation was  $\pm 10^\circ$ .

#### 4.2.3 Proposed Work

Supersonic wind tunnel tests will be continued to further improve the structural strength and to establish optimum geometry of the spiked parachutes. A number of runs will be made with the intent to validate the encouraging results of the experiments described above.

#### 4.3 Pressure Distribution Studies on Spiked Parachutes in Supersonic Flow

Progress Report No 19 presented results of pressure distribution studies on models of the spiked parachute at Mach 3.0. Figure 7-9 of that report showed a model to measure the pressure distribution throughout the wake area of the cone.

This model has now been tested, and the measurements reduced to coefficient form as described in Progress Report No 19, Sec 4.3. The results are presented in Table 7-1 and schematically in Fig 7-4, together with the pressure distributions on the canopy and the base of the cone which were determined previously.

During the next reporting period the pressure distribution models will be tested at Mach 2.0. Also, the models will be tested at Mach 2.0 and 3.0 with a forebody in order to investigate its influence upon the pressure distribution of the spiked parachute.

#### 4.4 Supersonic Wind Tunnel Studies of Spiked Ribbon Parachutes

##### 4.4.1 Introduction

In view of the success of the above spiked parachute, it appears that the "spike" concept might be applicable to ribbon parachute canopies. As a first step in this investigation, an

extensive series of water analogy tests was conducted on two-dimensional models of spiked ribbon parachute configurations as reported in Progress Report No 18, Project 10. Based on these studies, rigid models with geometric porosities of 20, 25, and 30 percent distributed evenly over the canopy were constructed as shown in Progress Report No 19, Figs 10-4 through 10-6. Design details of a typical model, together with nomenclature, are given in Fig 7-5. The models are shown in Fig 7-6.

#### 4.4.2 Tests

The rigid models above have been tested in a supersonic wind tunnel at Mach 3.0. The test arrangement is shown in Fig 7-7. During each test run, the stability is observed visually and recorded. Also, high speed Schlieren movies are made of each test. The cone is then moved to a new  $H/D_1$  position and the test is repeated. Thus the cone standoff distance is varied over the desired range for each model.

In order to investigate the effect of cone size, models were tested with  $34^\circ$  half angle cones, first with a base diameter  $d$  of 37% of the canopy inlet diameter  $D_1$  ("small"), and then with a base diameter of 47% of the inlet diameter ("large"). All configurations tested are listed in Table 7-2.

#### 4.4.3 Results

The criteria for the degree of stability in the rigid tests is a combination of the amplitude of vibration and the steadiness of the shock patterns as determined from analysis of the Schlieren movies. Stability of each configuration is noted in Table 7-2. The following general trends were found:

- a) As the porosity of the canopy was increased, overall stability of the flow pattern increased, especially in the region between the base of the cone and the canopy

- b) As the distance from the cone to the canopy was increased, stability of the flow pattern decreased.
- c) The models with the small cones were more stable than corresponding configurations with the large cones.

Figure 7-8 shows the characteristic flow pattern for the configuration which has so far displayed the best stability. Figure 7-9 presents a sequence from the schlieren movies which shows the extreme instability of the flow pattern typical of configurations with a forward cone position and low canopy porosity.

#### 4.4.4 Proposed Work

In view of the experiments described above, it appears to be advisable to conduct experiments with models of higher geometric porosity and with cone standoff distances of  $H/D_1$  from 0.45 to 0.615. Therefore, a model with a geometric porosity of 40 percent has been designed and fabricated as shown in Figs 7-6 and 7-10. If satisfactory results are obtained, a series of pressure distribution studies will be made.

CANOPY	INTERNAL	TAP NO.	Cp
	INTERNAL	1	1.712
		2	0.650
		3	0.876
		4	0.882
		5	1.041
		6	1.370
		7	1.103
	EXTERNAL	1	0.467
		2	0.362
		3	0.267
		4	0.057
		5	0
		6	-0.003
		7	-0.007
CONE		8	0.461
		9	0.461
		10	0.469
		11	
STING		12	0.37
		13	0.35
		14	0.36
		15	0.54
		16	0.80
		17	0.68
		18	0.37
		19	0.14

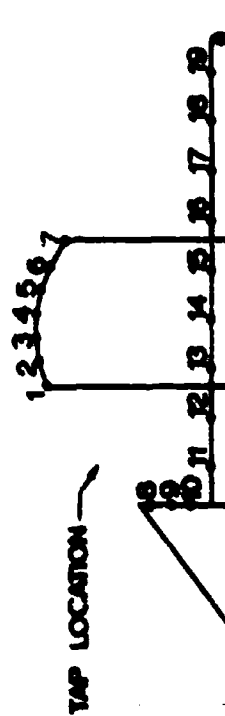


TABLE 7-1 PRESSURE COEFFICIENTS OF RIGID SPIKED PARACHUTE MODEL (WITHOUT SUSPENSION LINES)

TEST RUNS FOR MACH NO = 300				
POROSITY %	$H/D_1$	CONE SIZE	STABILITY	
20	.507*	Large		
	.615		Violently Unstable	
	.728		"	
	.838		"	
25	.507	Small	Unstable	
	.615		"	
	.728		"	
	.838		"	
30	.507	Large	"	
	.615		"	
	.728		"	
	.838		"	
30	0	No Cone		
	.507	Small	Violently Unstable	
	.615*			
	.728		Violently Unstable	
	.507	Large	Unstable	
	.615		Violently Unstable	
	.728		Moderately Unstable	
	.838		Unstable	
DATA NOT USED IS STARRED				

TABLE 7-2. RIGID SPIKED RIBBON PARACHUTE CONFIGURATIONS TESTED

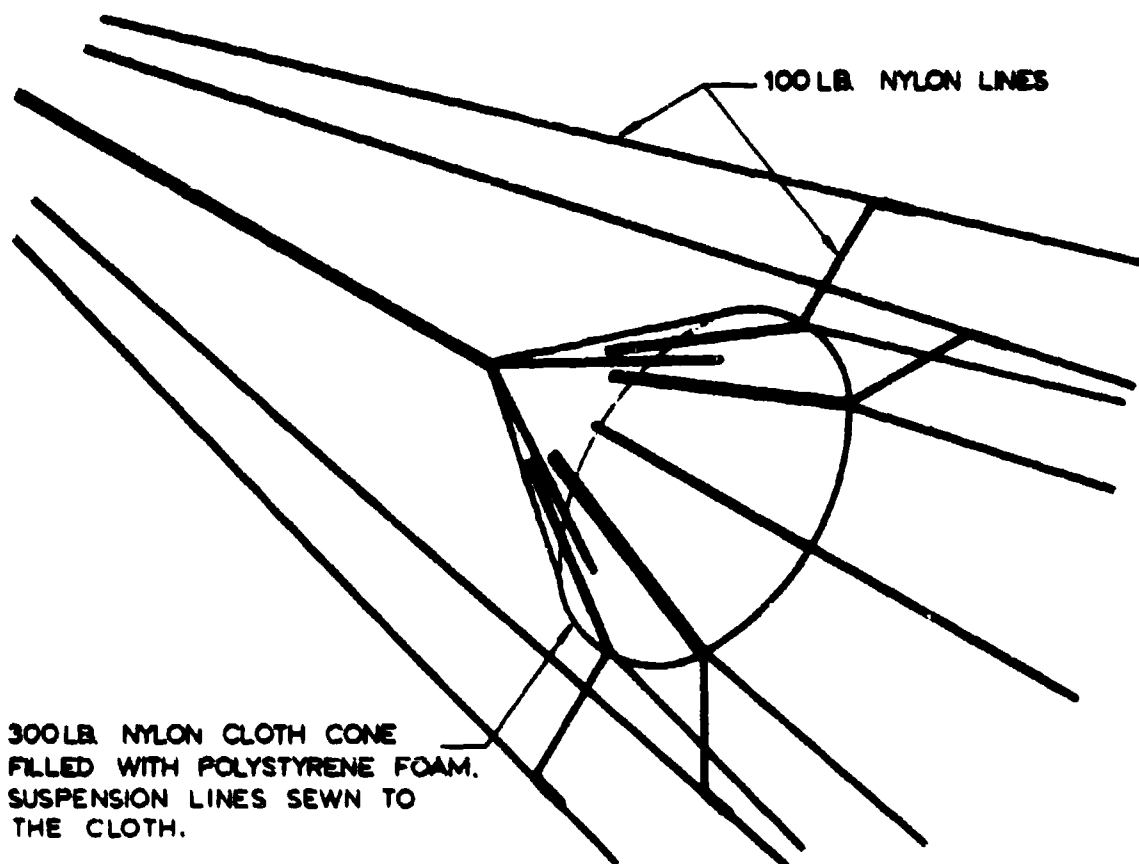


FIG 7-1. DETAIL OF MODIFIED CONE AND SUSPENSION LINE SYSTEM

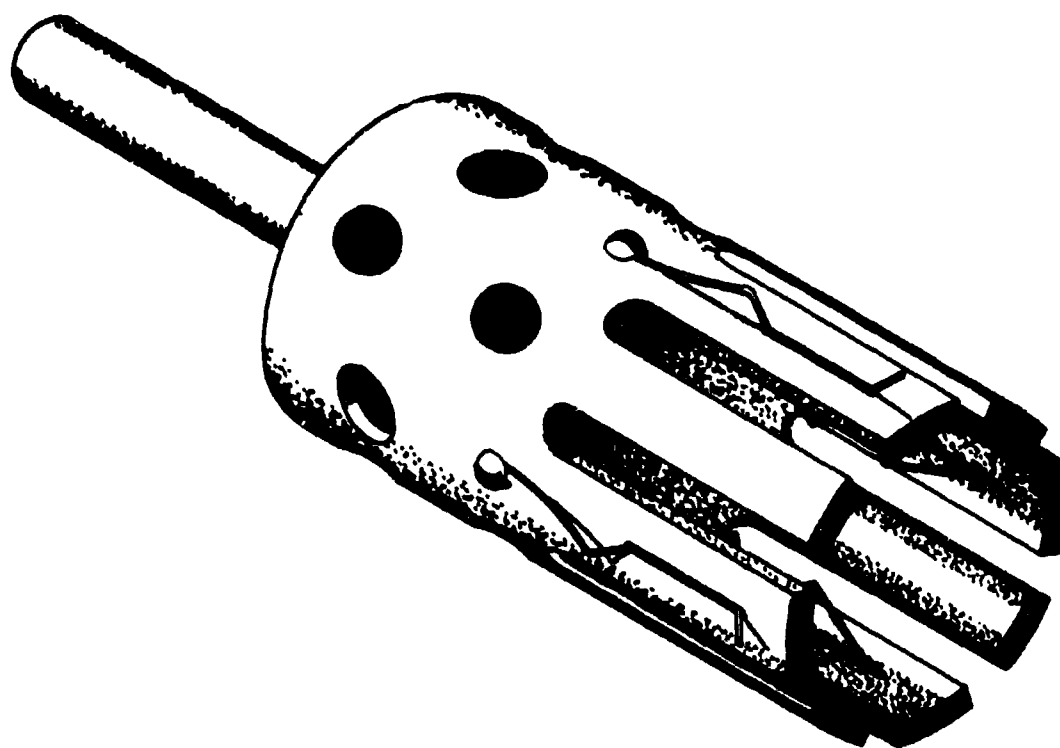


FIG 7-2. DISREEFING SYSTEM FOR SPIKED PARACHUTES



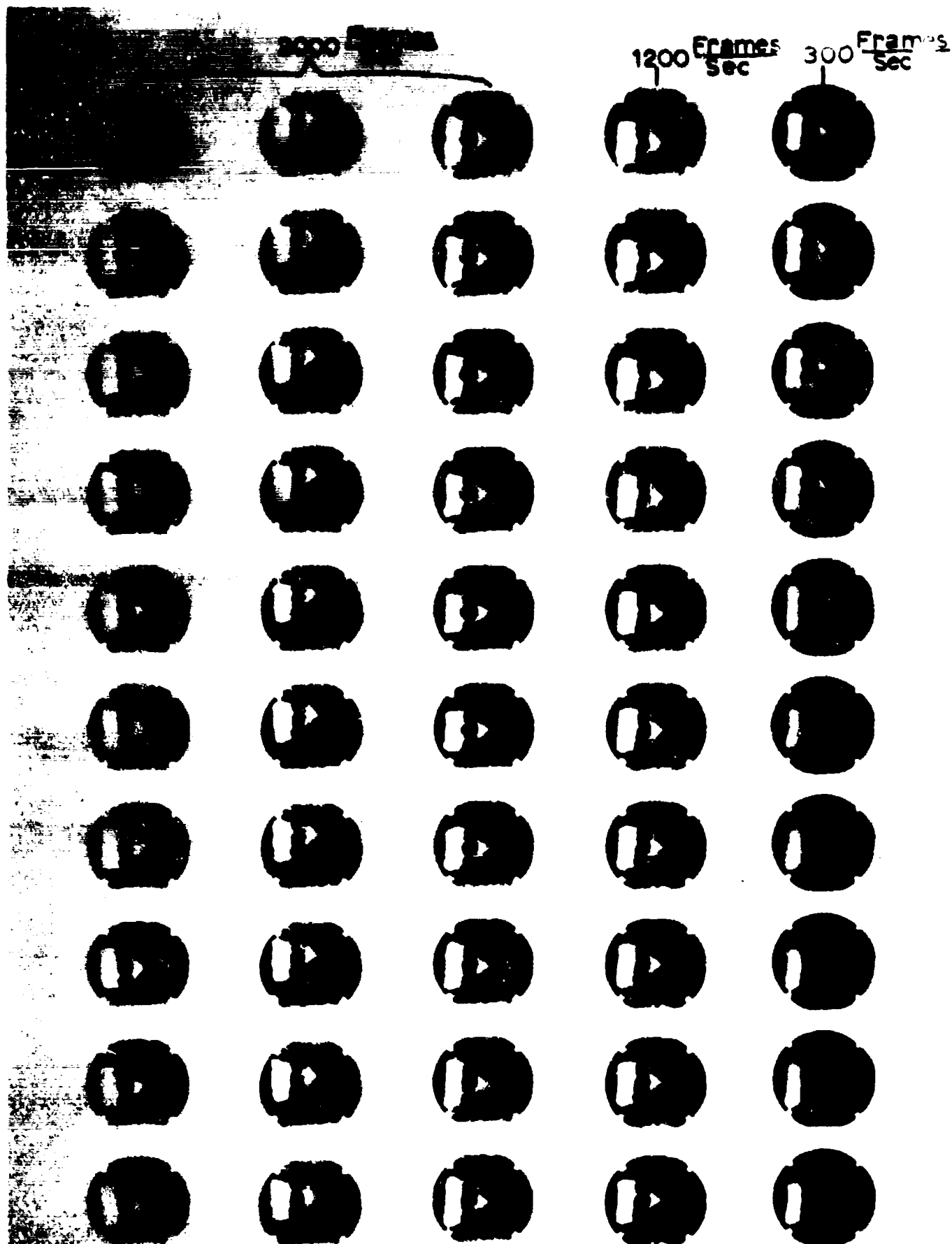


FIG 7-3. FLEXIBLE SPIKED PARACHUTE AT MACH 3.0.

300 LB/IN Nylon Canopy, Polystyrene Foam Cone.

$H/D_1 = 0.68$ ,  $D_0/D_1 = 0.90$ ,  $l/D_1 = 0.35$

( Sequence Taken at Intervals Over Entire Test Run)

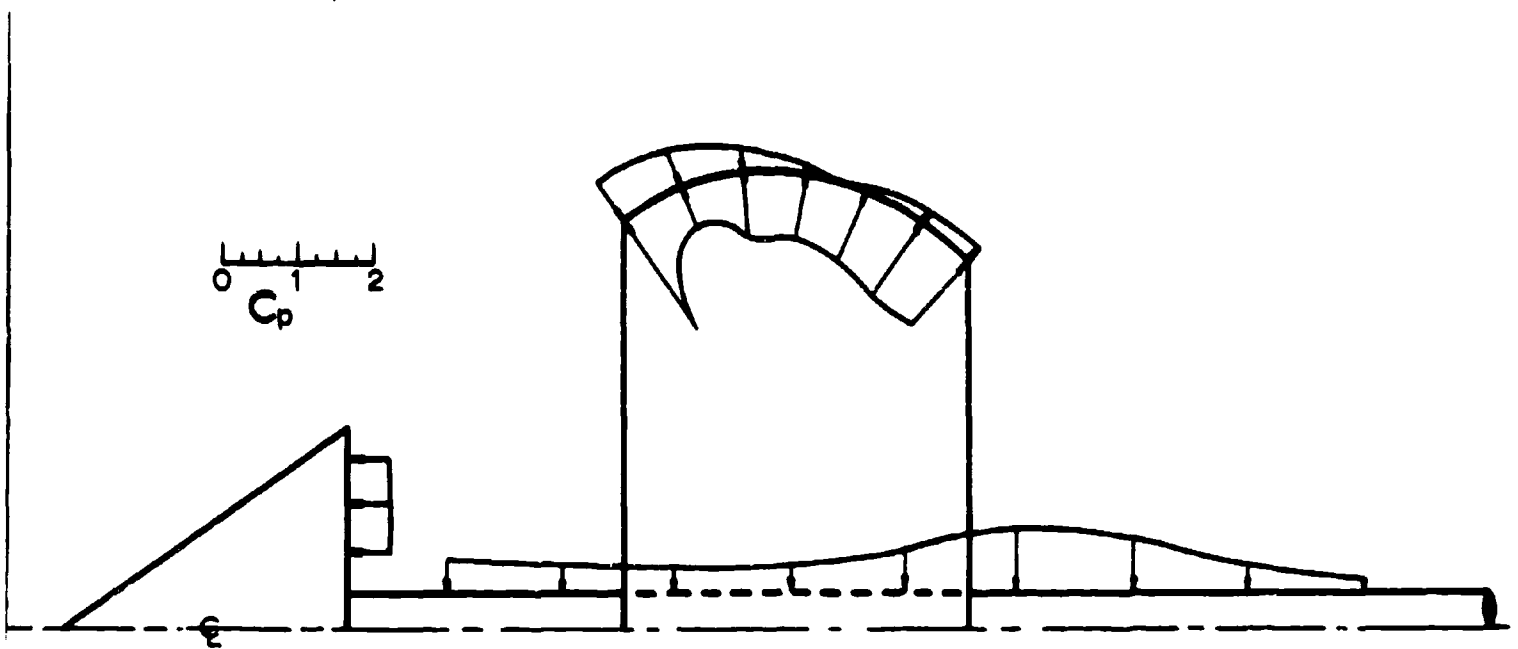


FIG 7-4. SCHEMATIC PRESSURE COEFFICIENT DISTRIBUTION ON RIGID SPIKED PARACHUTE MODEL (WITHOUT SUSPENSION LINES)

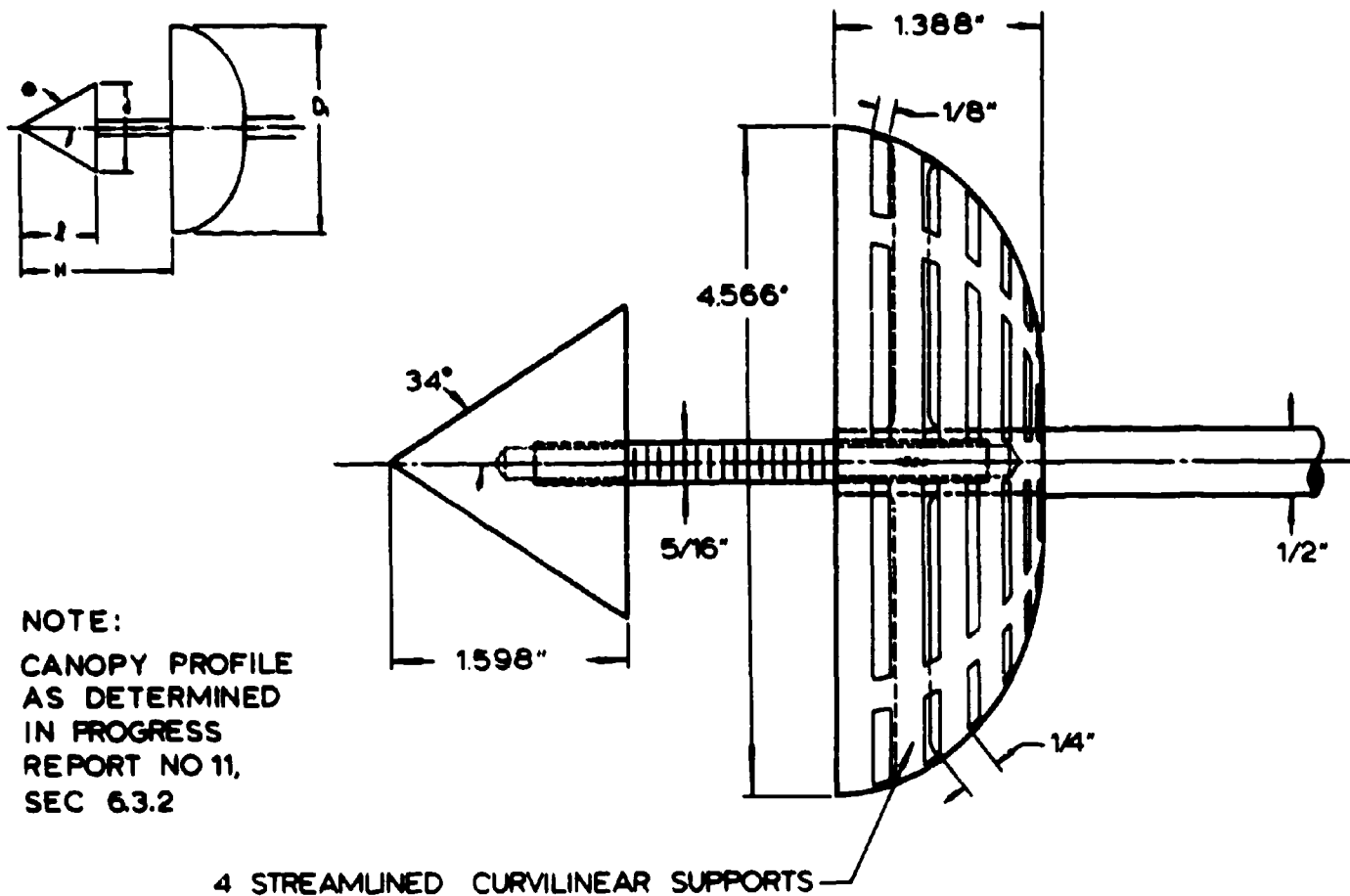


FIG 7-5. WORKING DRAWING OF SPIKED RIBBON PARACHUTE



FIG 7-6. RIGID MODELS OF SPIKED RIBBON PARACHUTES.

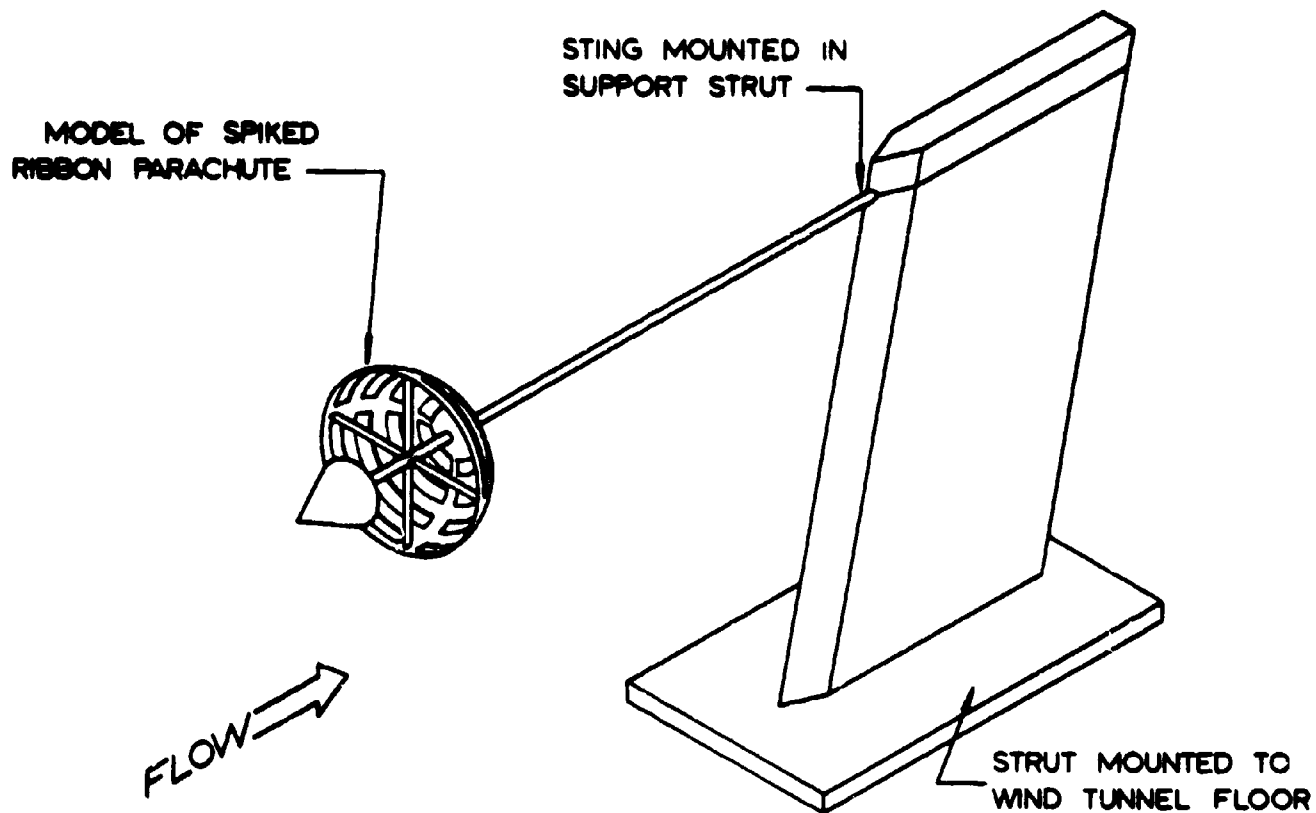


FIG 7-7. TEST ARRANGEMENT FOR RIGIDLY MOUNTED MODELS

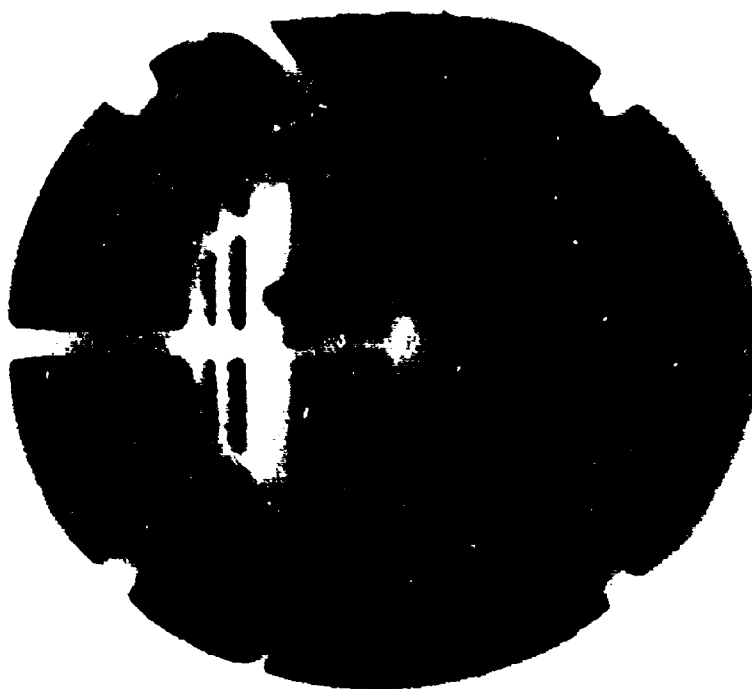


FIG 7-8. STABLE RIGID SPIKED RIBBON PARACHUTE  
AT MACH 3.0.  
 $H/D_1 = 0.51$ ,  $d/D_1 = 0.37$ , 30% Porosity



FIG 7-3. UNSTABLE RIGID SPOKED RIBBON PARACHUTE AT MACH 3.0.

$H/D_1 = 0.73$ ,  $d/D_1 = 0.37$ , 25% Porosity

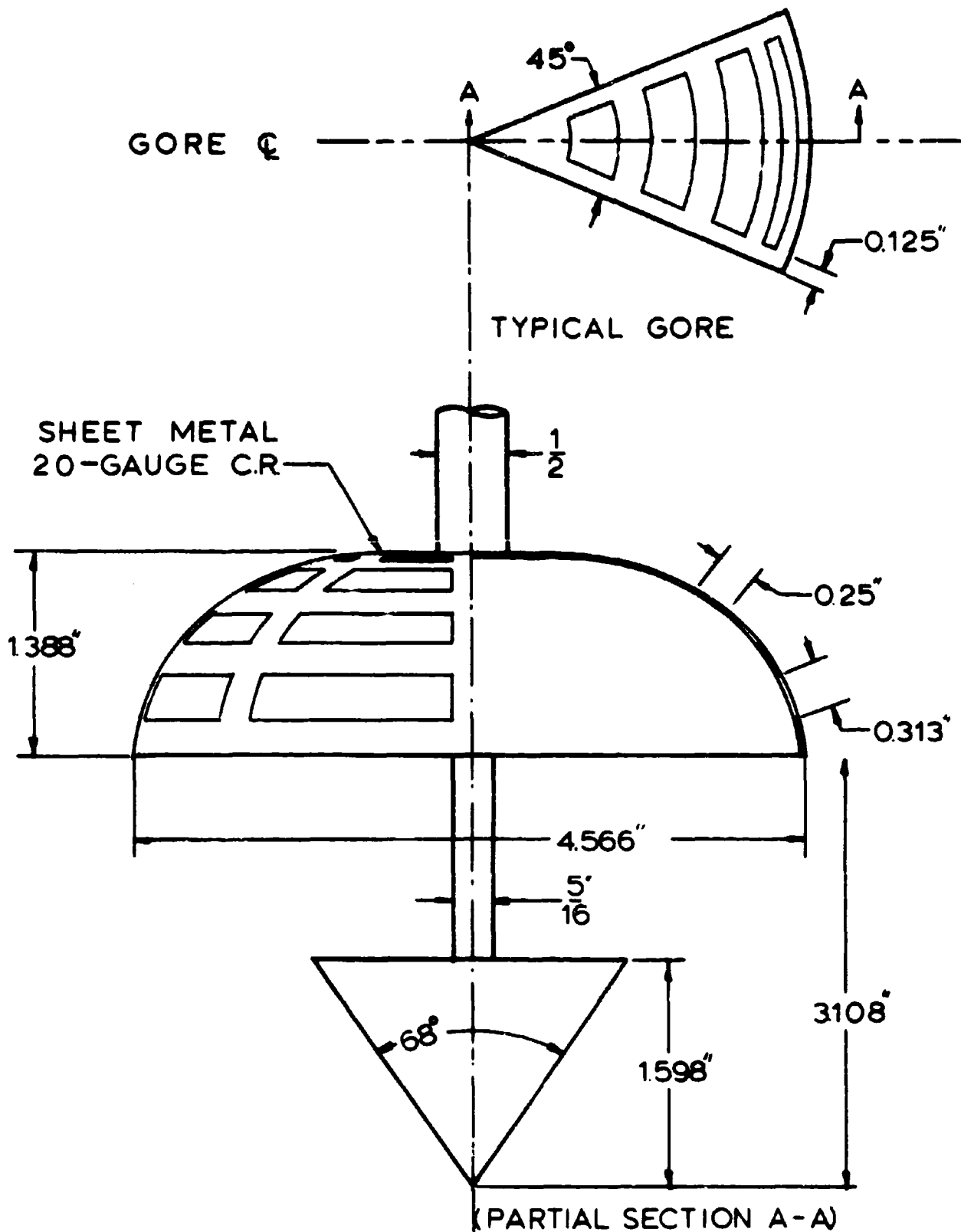


FIG 7-10. SPIKED RIBBON PARACHUTE CONFIGURATION (40% POROSITY)

## Project No 8

### 5.0      Theoretical Analysis of the Dynamics of the Opening Parachute

#### 5.1      Analytical Investigation of Parachute Inflation Time and Opening Force

No work has been done on this phase of the investigation during this reporting period.

#### 5.2      Size-Force History of an Inflating Parachute

The objective of this study is to experimentally justify the assumptions used in the analytical investigation above.

The first assumption, that the projected area varies parabolically with time, has been justified for a 3 ft nominal diameter circular flat parachute in the finite mass case. These results are presented in Progress Report No 18.

As stated in Progress Report No 19, further tests were made to investigate the second assumption, that the drag coefficient remains constant during the opening process. The data from these tests has now been reduced. However, it was found that further refinements in the testing apparatus were necessary.

These corrections have been made, and wind tunnel size-force-time studies will be resumed on models of circular flat and 10% flat extended skirt parachutes as soon as a high speed movie camera is available.

#### 5.3      Drag Studies on Reefed Canopies

An extensive wind tunnel study of drag of reefed canopies has been made, and the data has been reduced. These results are presently being analyzed and will be presented in the next progress report.

## Project No 9

### 6.0      Statistical Analysis of Extraction Time, Deployment Time, Opening Time, and Drag Coefficient for Aerial Delivery Parachutes and Systems

The second draft of the technical report for this project has been completed and is currently being reviewed.



## Project No 10

### 7.0      Study of Basic Principles of New Parachutes and Retardation Devices

In the last two progress reports, this project has been concerned with the investigation of the spike-ribbon parachute combination. However, since this investigation is so closely connected with the study of the spiked parachute which is presented under Project No 7, the spiked ribbon parachute study will now also be presented under that project.

## Project No 12

### 8.0      Gliding Aerodynamic Decelerator

#### 8.1      Introduction

The objective of this study is to develop a self-inflating aerodynamic decelerator which has a lift to drag ratio of 2. Pursuit of this objective involves investigation of present aerodynamically unstable parachutes and conventional steerable parachutes as well as new concepts in parachute design.

The forces and coordinates for a gliding parachute are shown in Fig 12-1. We see that for  $L/D = 2$ , the angle of attack of the parachute is

$$\begin{aligned}\alpha &= \tan^{-1} L/D \\ &= \tan^{-1} 2 \\ &= 63.5^\circ.\end{aligned}$$

Thus the parachute would glide at an angle of  $26.5^\circ$  to the horizon during descent.

#### 8.2      Experiments

##### 8.2.1      Conventional Steerable Parachutes

During this reporting period several models of unsymmetrical parachutes were tested in the open test section of the subsonic wind tunnel (Fig 12-2) or were dropped from low levels outdoors in still air in order to establish their stable angle of attack. The test section velocity in the wind tunnel tests varied from 17 to 25 ft/sec, while the vertical velocity in drop tests was approximately 13 ft/sec. The results of these tests are as follows:

- a) A 26 inch nominal diameter circular flat canopy with two double-sized slanted and five straight personnel guide surface-type extensions shown

in Fig 12-3 was stable at  $6^\circ \pm 2^\circ$  angle of attack, giving a glide angle with the horizon of approximately  $84^\circ$

- b) A 70 inch nominal diameter MC-1 extended skirt canopy modified with diametrically opposite slanted and vented extensions shown in Fig 12-4 exhibited a stable angle of attack in drop tests of  $21.5^\circ$ , giving a glide angle with the horizon of  $68.5^\circ$
- c) A 26 inch nominal diameter T-10 extended skirt canopy modified with an unsymmetrical arrangement of personnel guide surface-type extensions shown in Fig 12-5 was stable at  $12^\circ \pm 3^\circ$ , giving a glide angle with the horizon of  $78^\circ \pm 3^\circ$
- d) An unsymmetrical parachute with the gore pattern shown in Fig 12-7 was stable at  $38^\circ \pm 3^\circ$  angle of attack as shown in Fig 12-6, thus giving a glide angle with the horizon of  $52^\circ \pm 3^\circ$ ; however, full inflation could not be maintained in the test section as shown in Fig 12-6.

We see that none of these parachutes achieve a glide angle of 26.5 degrees with the horizon. Further existing glide parachutes will be studied as soon as models or other pertinent information is obtained.

### 8.2.2      Conceived Gliding Parachute

Progress Report No 18, Sec 9.3.3, reported that the desired glide angle has been achieved in the wind tunnel using balsa wood models modified with Plastilina modelling clay. During this reporting period the most favorable of those models, a modified 10% extended skirt canopy (T-10) was further modified as shown in Figs 12-8 and 12-9 in an attempt to achieve a configuration which could be fabricated from non-rigid materials. The two proposed shapes are similar with the exception that Model 2 (Fig 12-9) has a cut-out area in the rear of the canopy,

forming an exhaust jet area. These models were constructed of balsa wood and Plastilina and tested in the wind tunnel as shown in Figs 12-10 and 12-11. Results are as follows:

- a) Model 1 (Fig 12-8) was stable at  $48^\circ$  angle of attack, giving a glide angle with the horizon of  $42^\circ$
- b) Model 2 (Fig 12-9) achieved a stable angle of attack of  $56^\circ$ , giving a glide angle with the horizon of  $34^\circ$ .

It can be seen that these models come close to the required glide angle.

An attempt was made to construct flexible canopies with the shape of Model 2. Although these canopies were only approximately the desired shape, it was hoped to obtain preliminary information about the stable angle of attack. The first model was made from paper, and was approximately 18 inches in diameter. This model achieved a stable glide angle against the horizon of  $27^\circ$ . A second model the same size was made from nylon cloth with a nominal porosity of  $90 \text{ ft}^3/\text{ft}^2\text{-min}$ . This model was stable at  $43^\circ$  angle of attack, giving a glide angle of  $47^\circ$ .

In order to obtain accurate gore patterns for the above models, a 24 inch nominal diameter 10% extended skirt canopy was formed from wood. This basic model is being fitted with ribs of the desired shape as shown in Fig 12-12. From this model, it will be possible to obtain gore patterns of the proposed gliding parachute. This will be done during the next period, and textile models of the proposed decelerator will be built and tested in the wind tunnel.

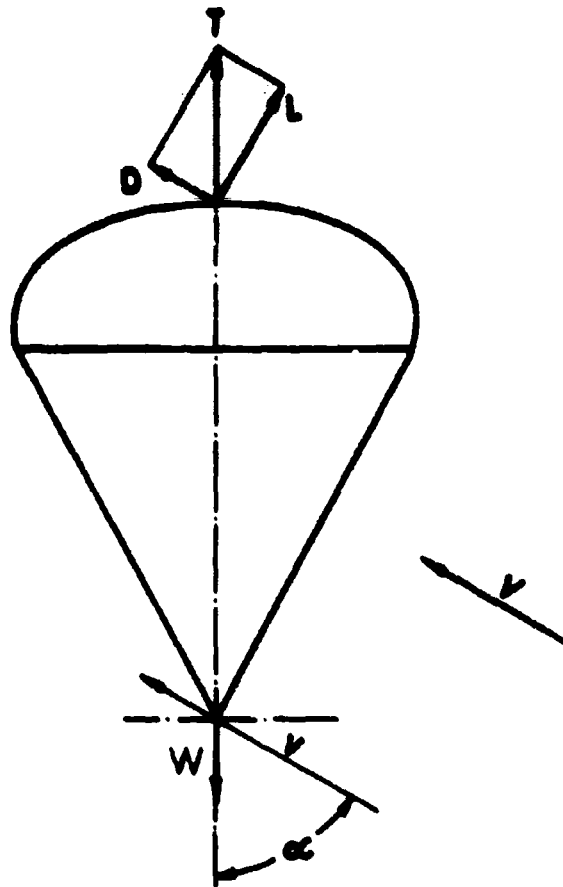


FIG 12-1. FORCES AND COORDINATES FOR A GLIDING PARACHUTE

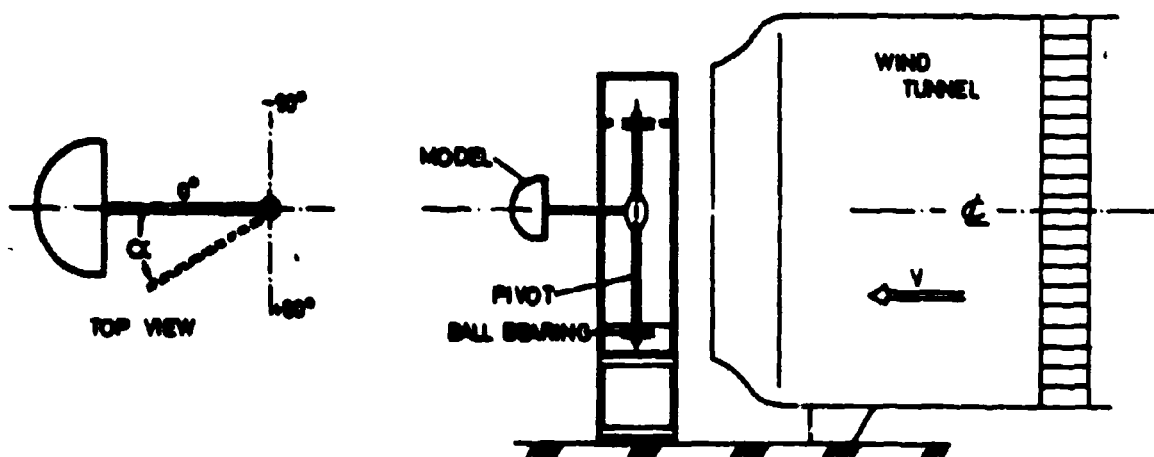


FIG 12-2. WIND TUNNEL TEST ARRANGEMENT

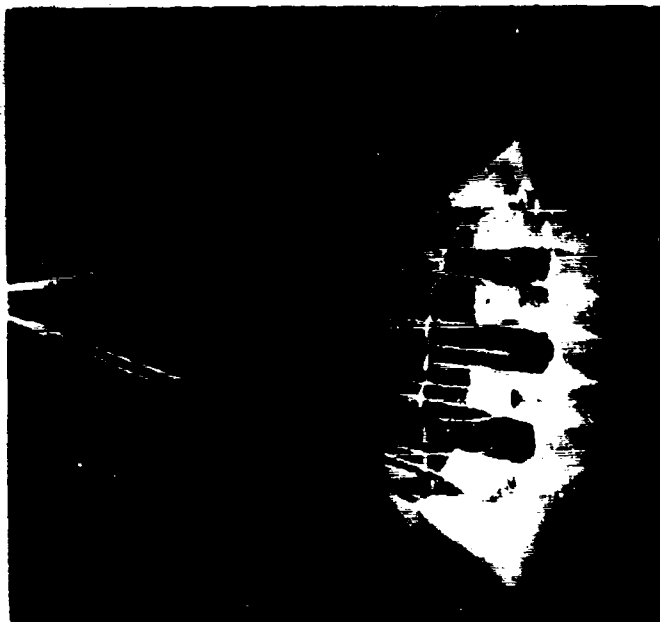


FIG 12-3. 26 INCH NOMINAL DIAMETER CIRCULAR FLAT PARACHUTE MODIFIED WITH EXTENSIONS IN WIND TUNNEL.

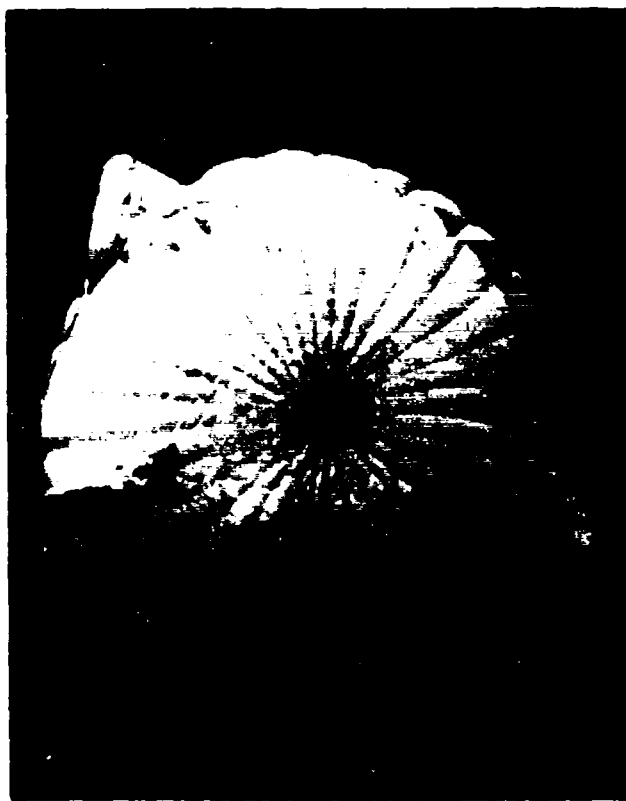


FIG 12-4. 70 INCH NOMINAL DIAMETER MC-1 EXTENDED SKIRT CANOPY MODIFIED WITH EXTENSIONS IN DROP TEST.

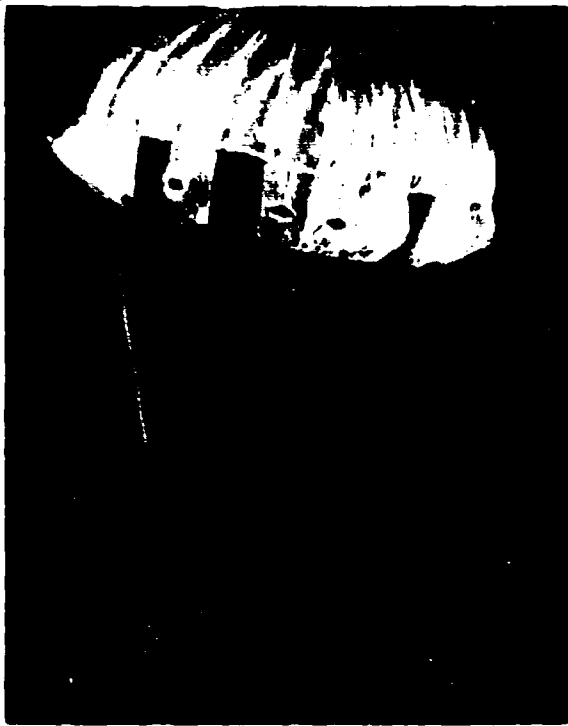
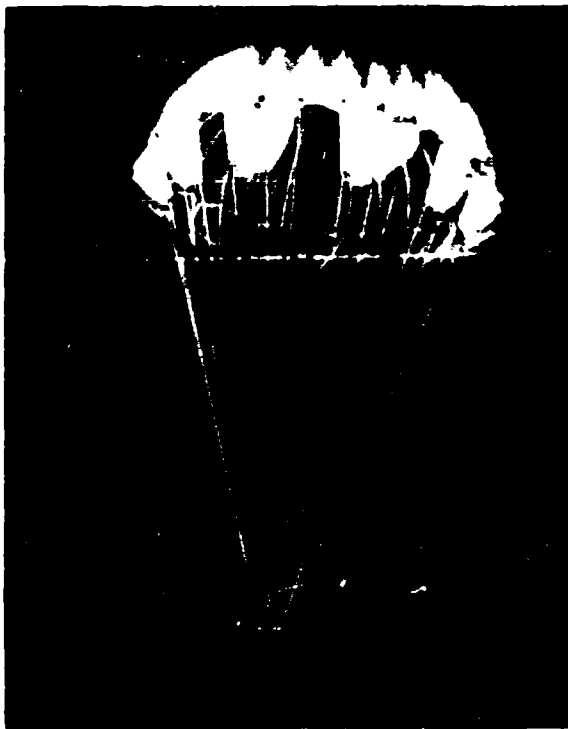
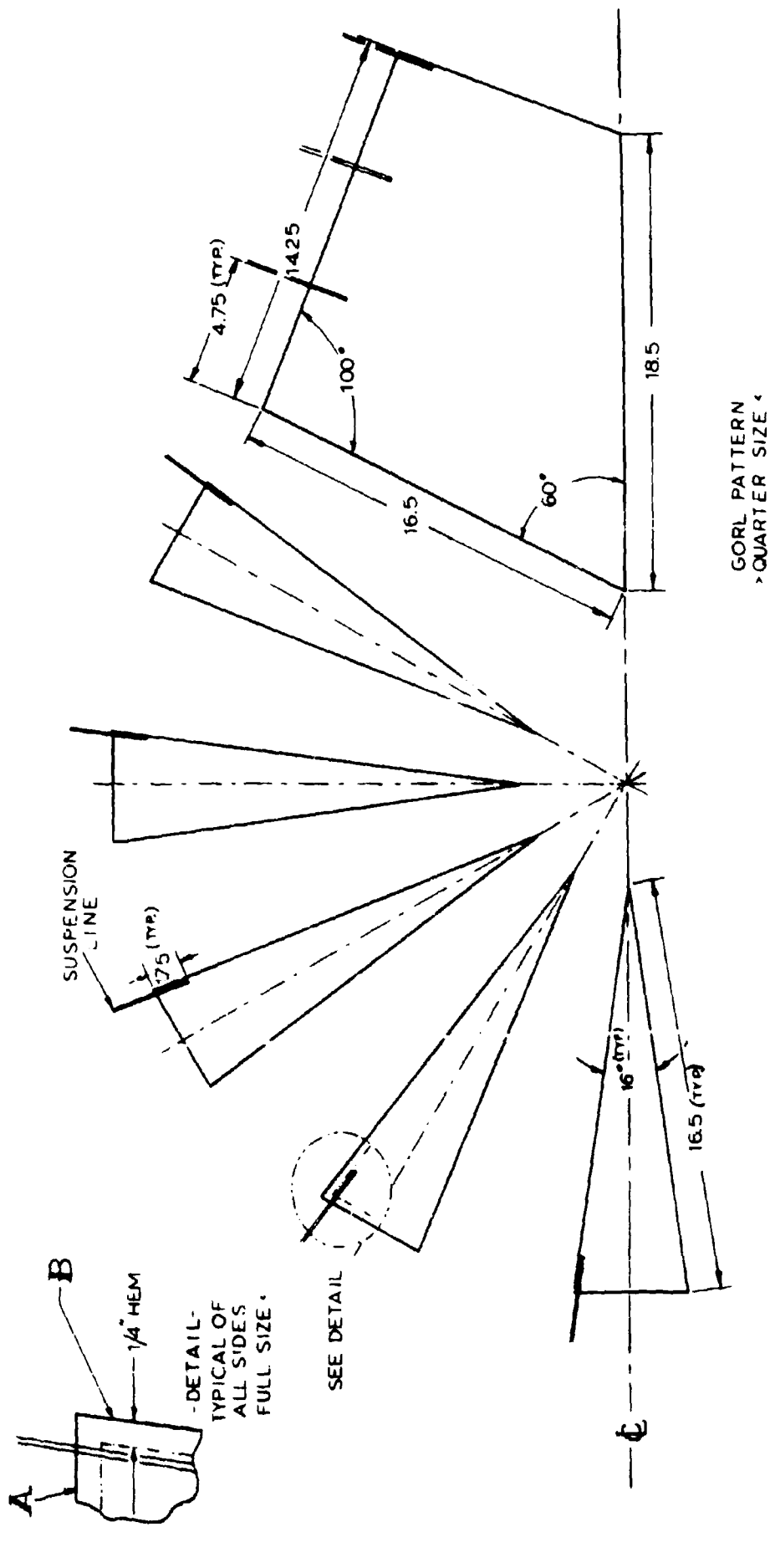


FIG 12-5. 26 INCH NOMINAL DIAMETER T-10 EXTENDED SKIRT PARACHUTE WITH UNSYMMETRICAL EXTENSIONS IN WIND TUNNEL.



FIG 12-6. UNSYMMETRICAL PARACHUTE IN WIND TUNNEL. INFLATION NOT MAINTAINED.



> NOT TO SCALE <

FIG 12-7. UNSYMMETRICAL PARACHUTE GORE PATTERN — 32 INCH NOMINAL DIAMETER



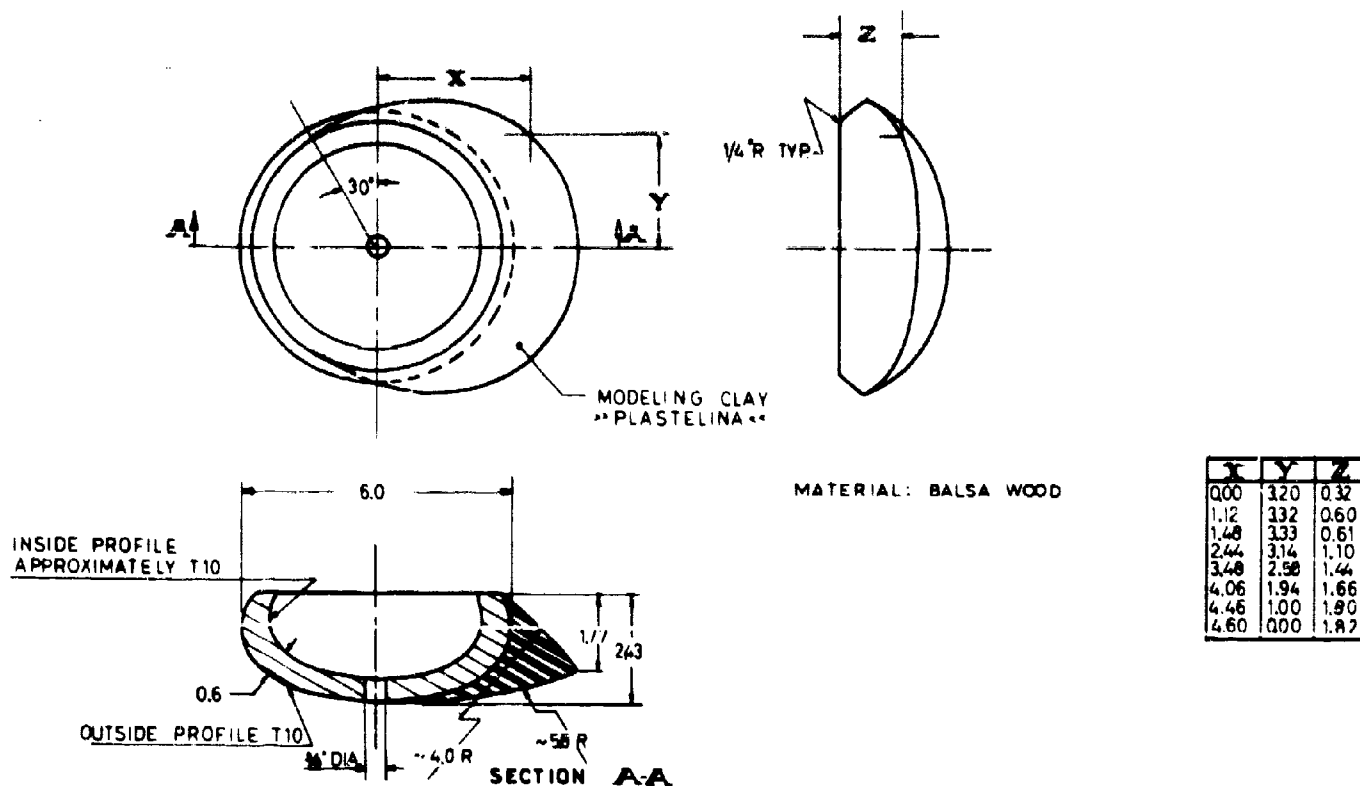


FIG 12-8. MODEL 1—GLIDING PARACHUTE MODIFIED FROM 10% EXTENDED SKIRT PARACHUTE

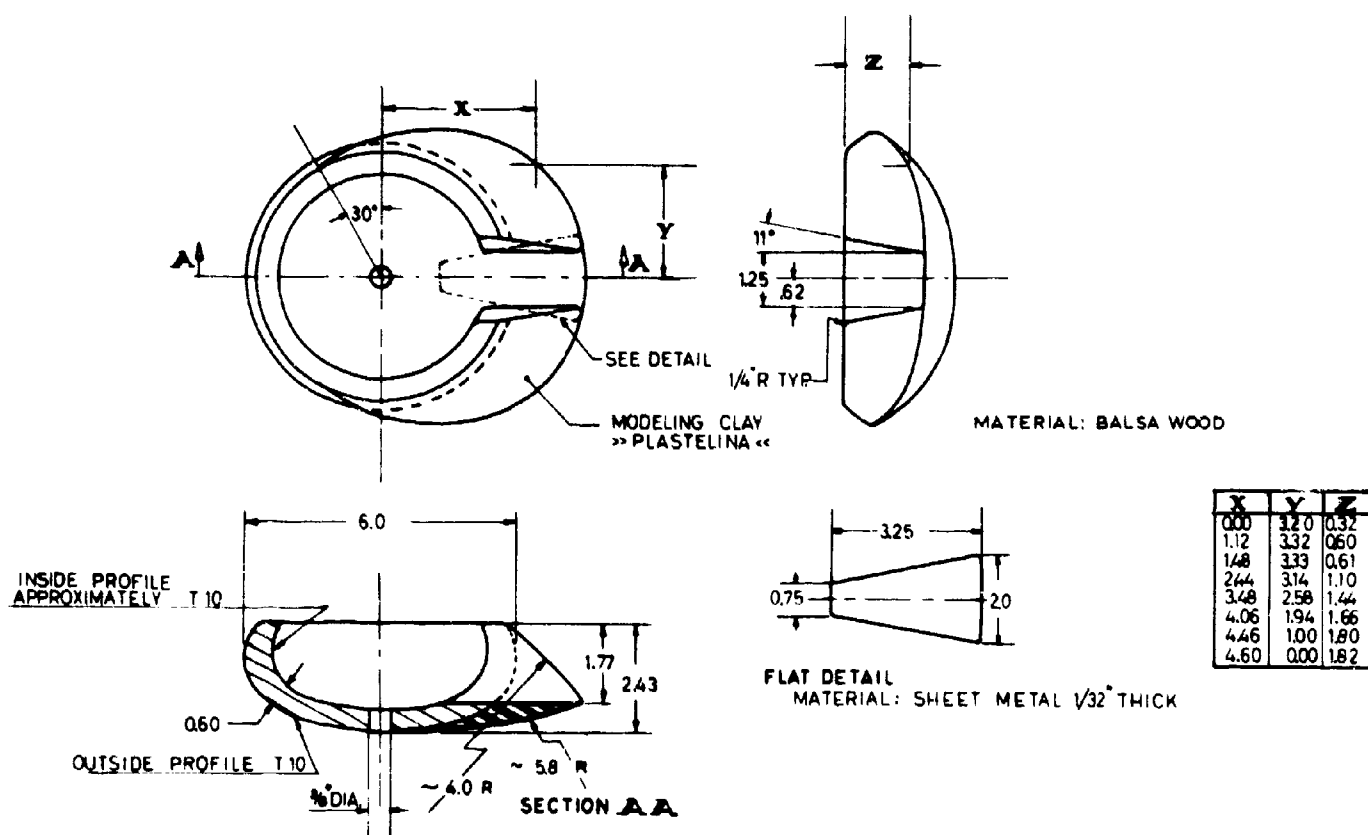


FIG 12-9. MODEL 2—GLIDING PARACHUTE MODIFIED FROM 10% EXTENDED SKIRT PARACHUTE

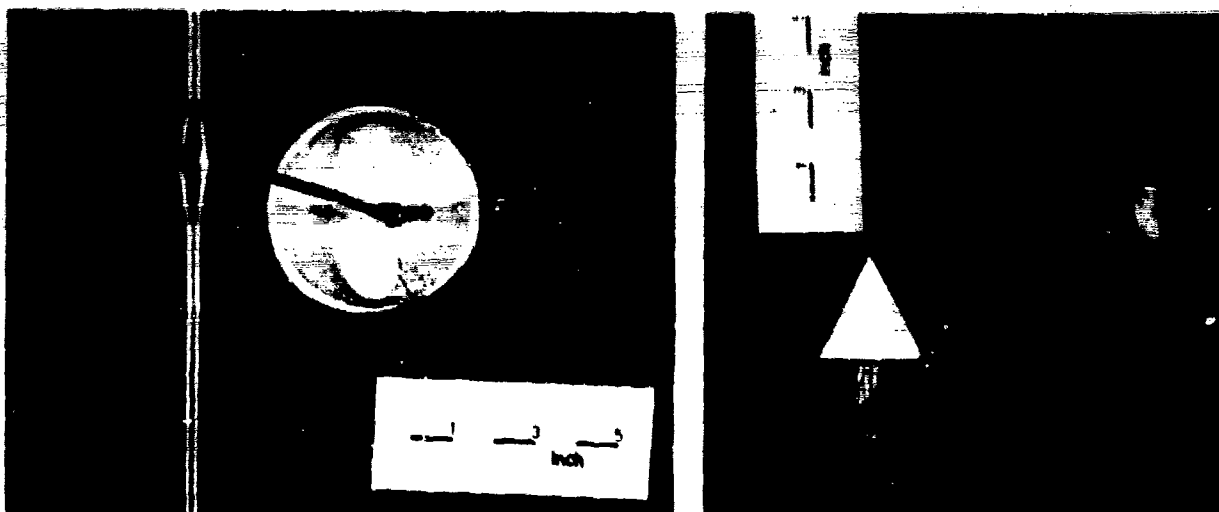


FIG 12-10. MODEL 1 - MODIFIED T-10 EXTENDED SKIRT CANOPY IN WIND TUNNEL.

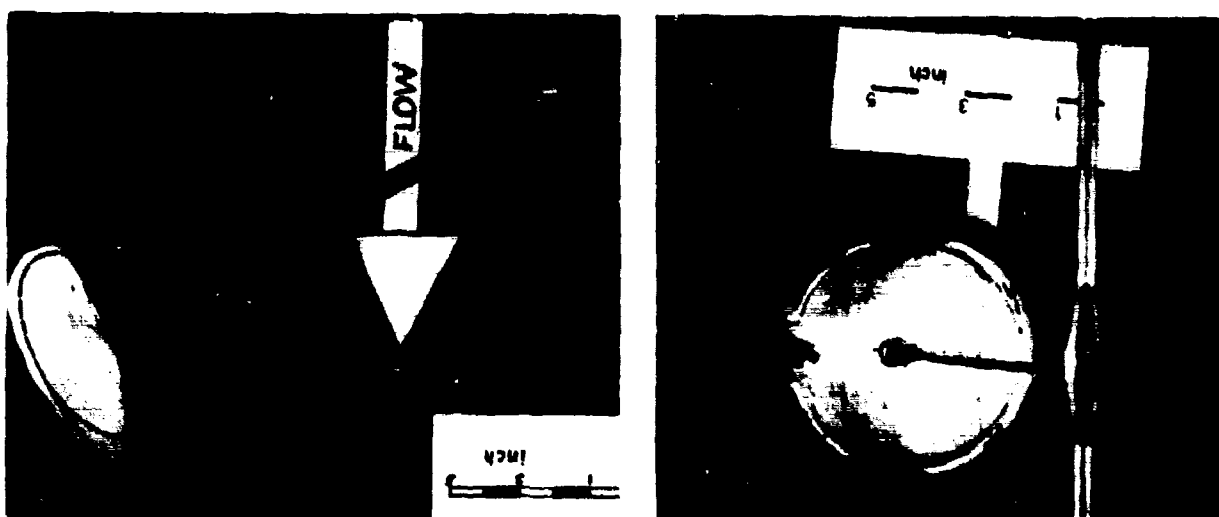


FIG 12-11. MODEL 2 - MODIFIED T-10 EXTENDED SKIRT CANOPY IN WIND TUNNEL.



FIG 12-12. 24 INCH NOMINAL DIAMETER 10% EXTENDED SKIRT CANOPY FOR OBTAINING GORE PATTERN OF GLIDING PARACHUTE.

## Project No 13

### 9.0      Effective Porosity Studies

Note: This project, which was formerly titled "Ribbon Grids for Supersonic Flow," now includes also the effective porosity studies of parachute cloths which were previously presented under Project No 4.

### 9.1      Parachute Cloths

#### 9.1.1      Introduction

Porosity studies of four common parachute cloths for sub-critical pressure ratios and altitudes above 50,000 ft have been presented previously. Progress Report Nos 16 and 18 gave details of a facility which was capable of extending the test range for cloths over a density range of  $0.10 \leq \sigma \leq 1$  and a pressure ratio range of  $0.05 \leq \Delta P / \Delta P_{cr} \leq 2.0$ .

In the course of experimentation, it was found that the shape and size of the cloth specimen, as well as the particular piece of cloth tested, influenced significantly the test results. Also, the cloth stretched and slipped in the test holder, introducing elasticity effects and a variation in sample area during testing.

9.1.2      To investigate the effects of these mechanical details, a new set of standard test samples was constructed. A sample of each cloth was bonded with epoxy resin to a 2 inch internal diameter brass ring as shown in Fig 13-1. The circular shape provides the minimum stress in the cloth for any given pressure, thereby also reducing the elasticity effects. Bonding the samples permanently to the ring eliminates slippage, and the corresponding area variations.

These standard samples have been tested over the density and pressure ranges specified above. All pressure measurements were made with U-tube manometers containing fluids with specific gravities ranging from 0.81 to 13.5, in order to obtain maximum sensitivity for all pressure ratios.

### 9.1.3 Results

Approximately four tests of each sample were made at constant downstream  $\sigma$  values varying over the density range specified above. Figures 13-2 through 13-5 present the effective porosity  $C$  of the four materials versus pressure ratio  $\Delta p / \Delta p_{cr}$  with  $\sigma$  as a parameter. These curves represent average values of the tests at each  $\sigma$ . The results vary slightly from previously presented results due to the model effects mentioned above. However, established trends are followed. It is seen that the effective porosity decreases with decreasing  $\sigma$ . With the improved experimental arrangement, values in the lower pressure ratio range appear to be quite reliable, and it can be seen that in general the slope of  $C$  versus  $\Delta p / \Delta p_{cr}$  is positive to a certain point and then becomes negative. This seems to indicate that the air resistance of the cloth increases as the Reynolds number increases until the compressibility effects become more influential, and the effective porosity then decreases with a further increase of the differential pressure.

The preceding test results are merely a validation of earlier experiments and may be considered as a check and a refinement of previous information. Notification will be given if significant new findings should occur. The further research will proceed on a relatively low priority basis.

### 9.2 Ribbon Grid Configurations

Progress Report No 19 presented results of a series of effective porosity tests of parallel ribbon configurations at

sea level density. Models were made both from steel and from nylon ribbons, and results were compared and analyzed to determine the effects of the deformation of the textile models.

During this reporting period, effective porosity tests were made on a series of ribbon grid configuration fabricated from steel shim stock. A typical model layout of these configurations is shown in Fig 13-6. Figure 13-7 shows several steel and nylon ribbon grid models. All models have a geometric porosity of 25%. Configuration changes were made by varying the included angle  $\theta$  between the ribbons, with values of 90, 75, 60, 45, 30, and 15 degrees chosen. Also included in this test series is a model with parallel ribbons  $3/8$  inch wide.

A corresponding set of models has been fabricated from MIL-R-5608B, Class B,  $1/4$  inch wide nylon ribbon. Effective porosity tests have also been made on these models, together with a sequence of photographs showing simultaneous front and side views of the model during the test run. However, data reduction and evaluation on these tests has not been completed.

Figure 13-8 presents the effective porosity of the seven steel configurations as a function of pressure differential at sea level density. These curves present average values from two or more runs. It can be seen that the shape of the grid as expressed in the included angle has a definite effect on the effective porosity. Furthermore, the effective porosity decreases with increasing differential pressure, somewhat similar to those observed in the studies of solid cloth samples.

During the next reporting period, data reduction and evaluation of the tests on the nylon ribbon grid models will be completed, with emphasis placed on determining the effect of the deformation on the effective porosity. Also, all steel and nylon parallel ribbon and ribbon grid models will be tested at density ratios  $\sigma < 1$ .

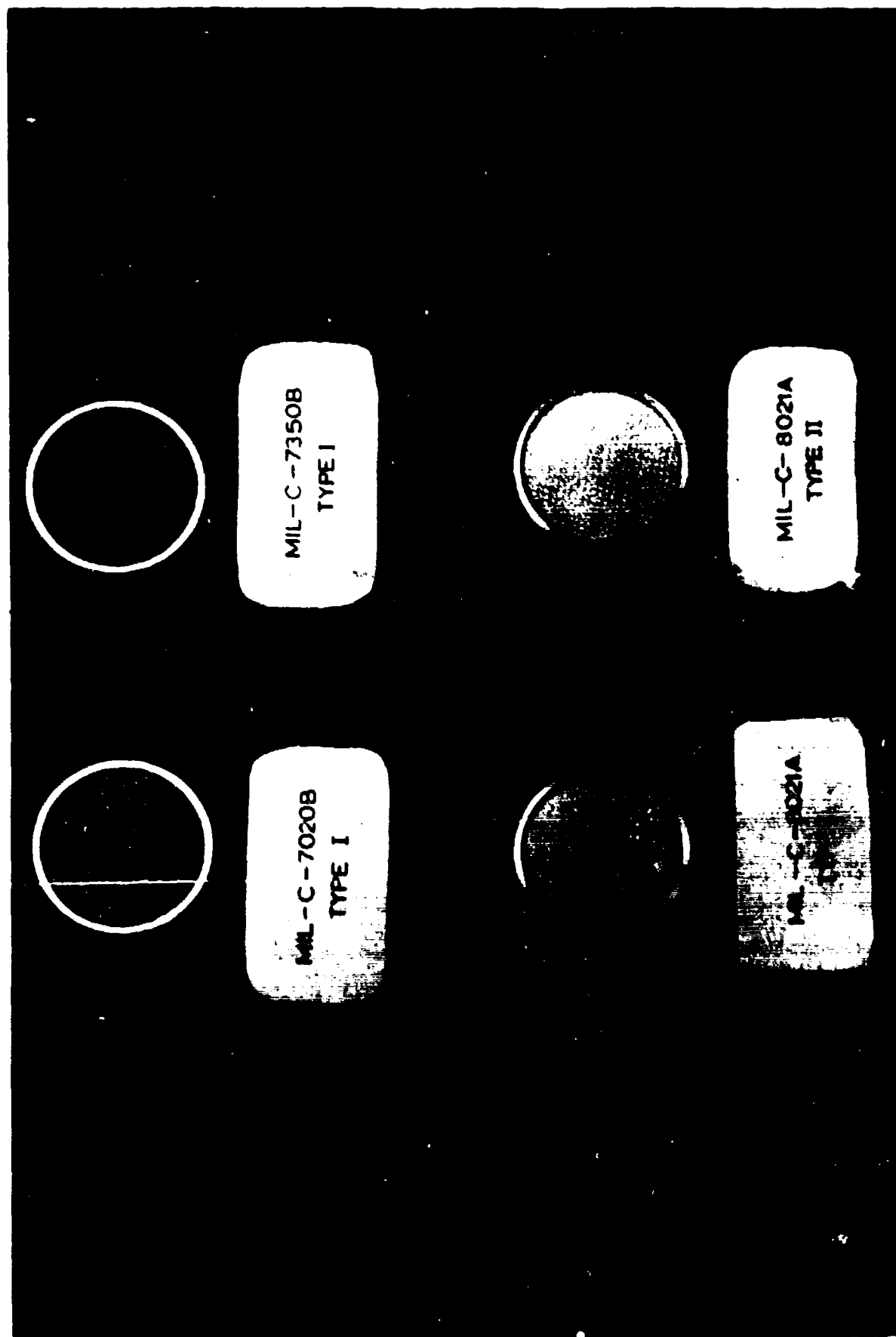


FIG 13-1. STANDARD TEST SAMPLES OF PARACHUTE CLOTHS FOR EFFECTIVE POROSITY STUDIES

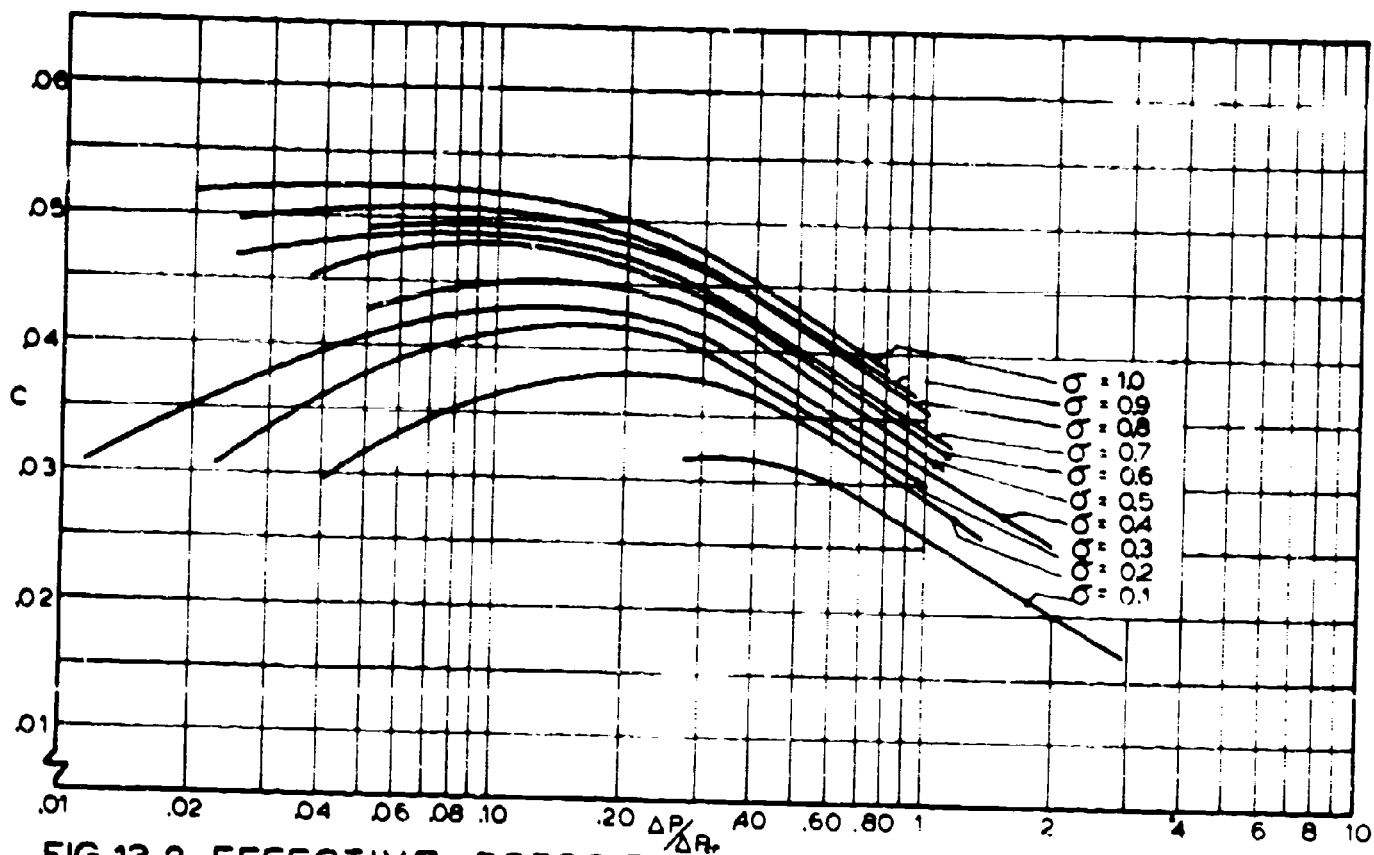


FIG 13-2. EFFECTIVE POROSITY VERSUS PRESSURE RATIO  
MIL-C-7020B, TYPE I, 40 LB/IN

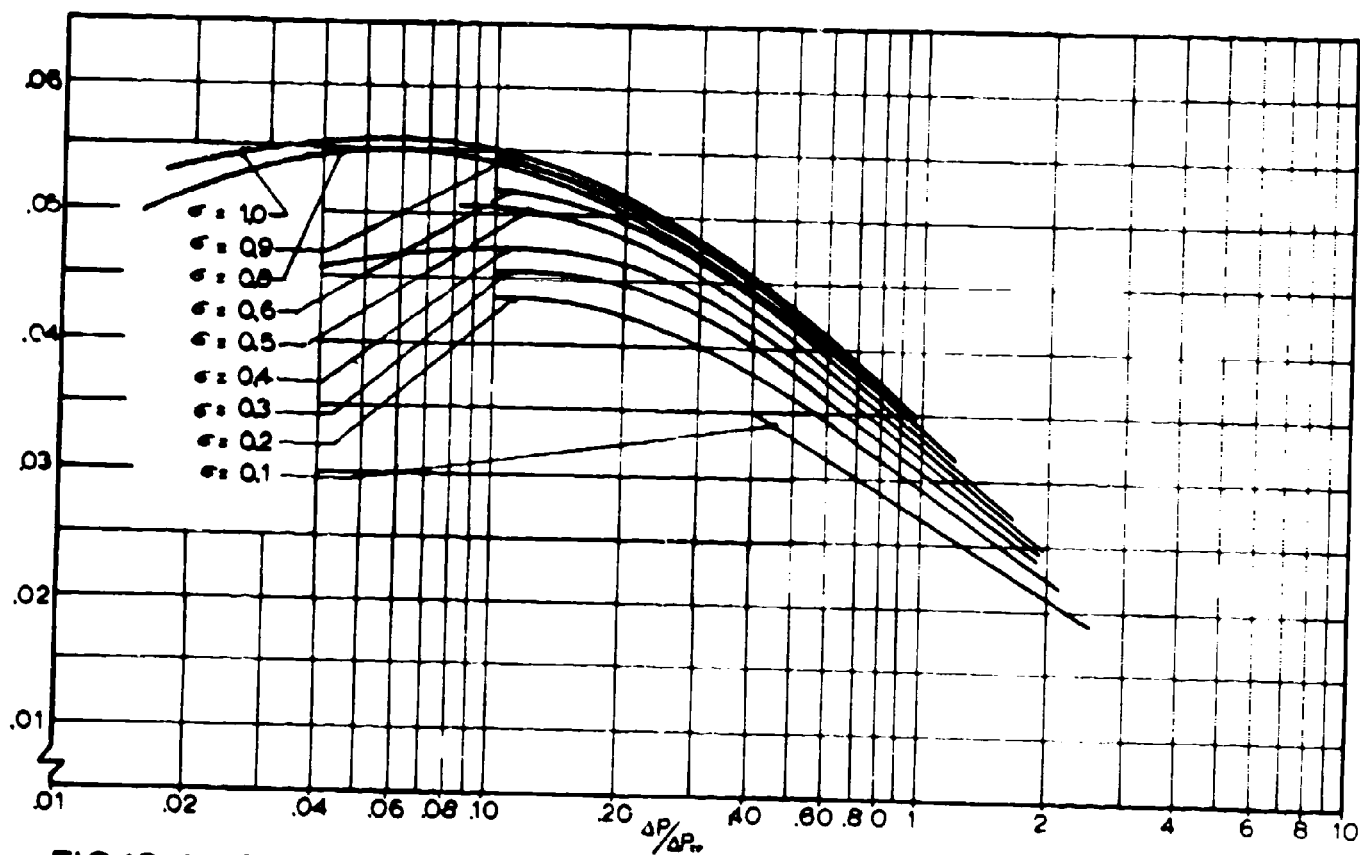


FIG 13-3 EFFECTIVE POROSITY VERSUS PRESSURE RATIO  
MIL-C-7350B, TYPE I, 90 LB/IN

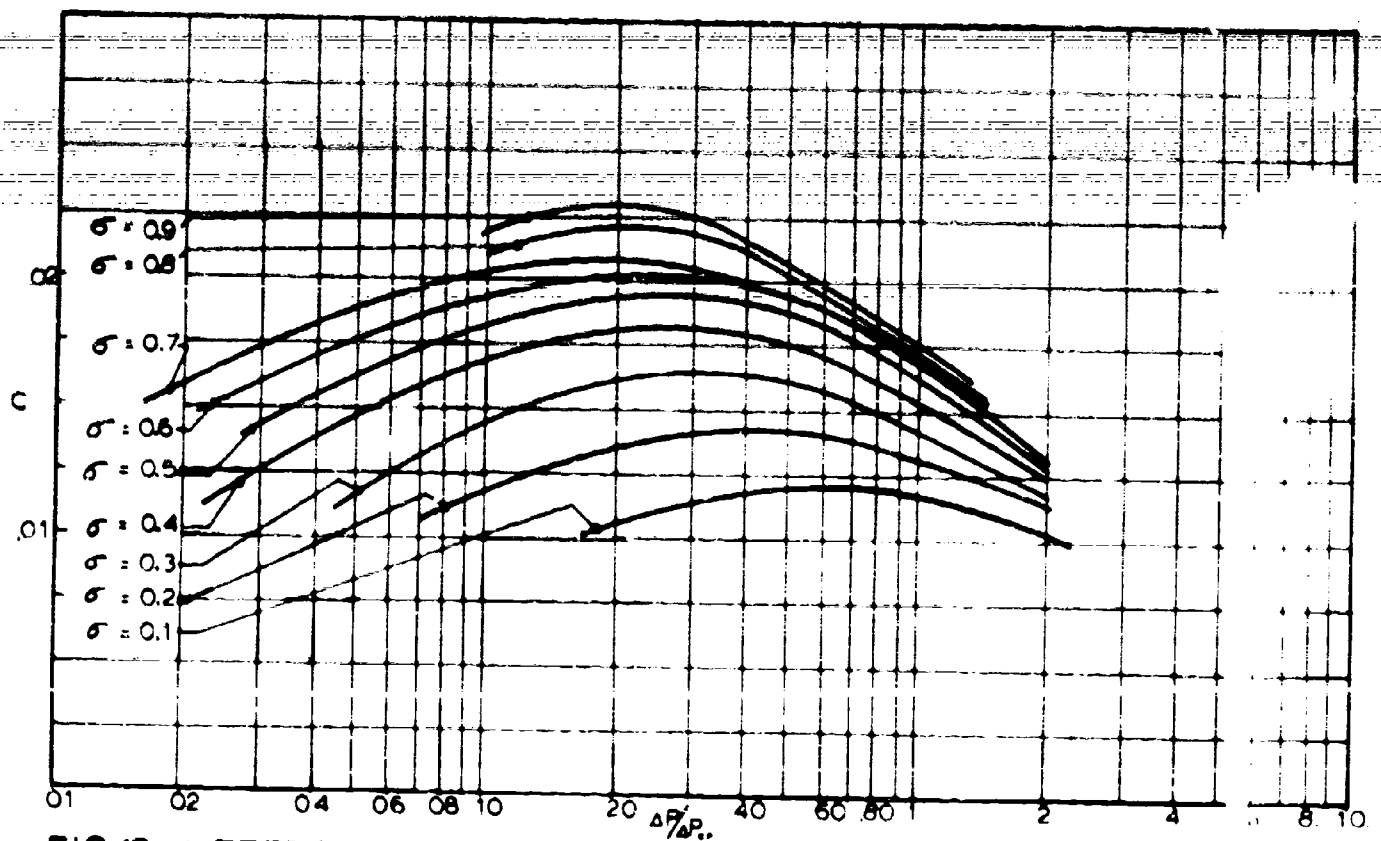


FIG 13-4. EFFECTIVE POROSITY VERSUS PRESSURE RATIO  
MIL-C-8021A, TYPE I, 200 LB/IN

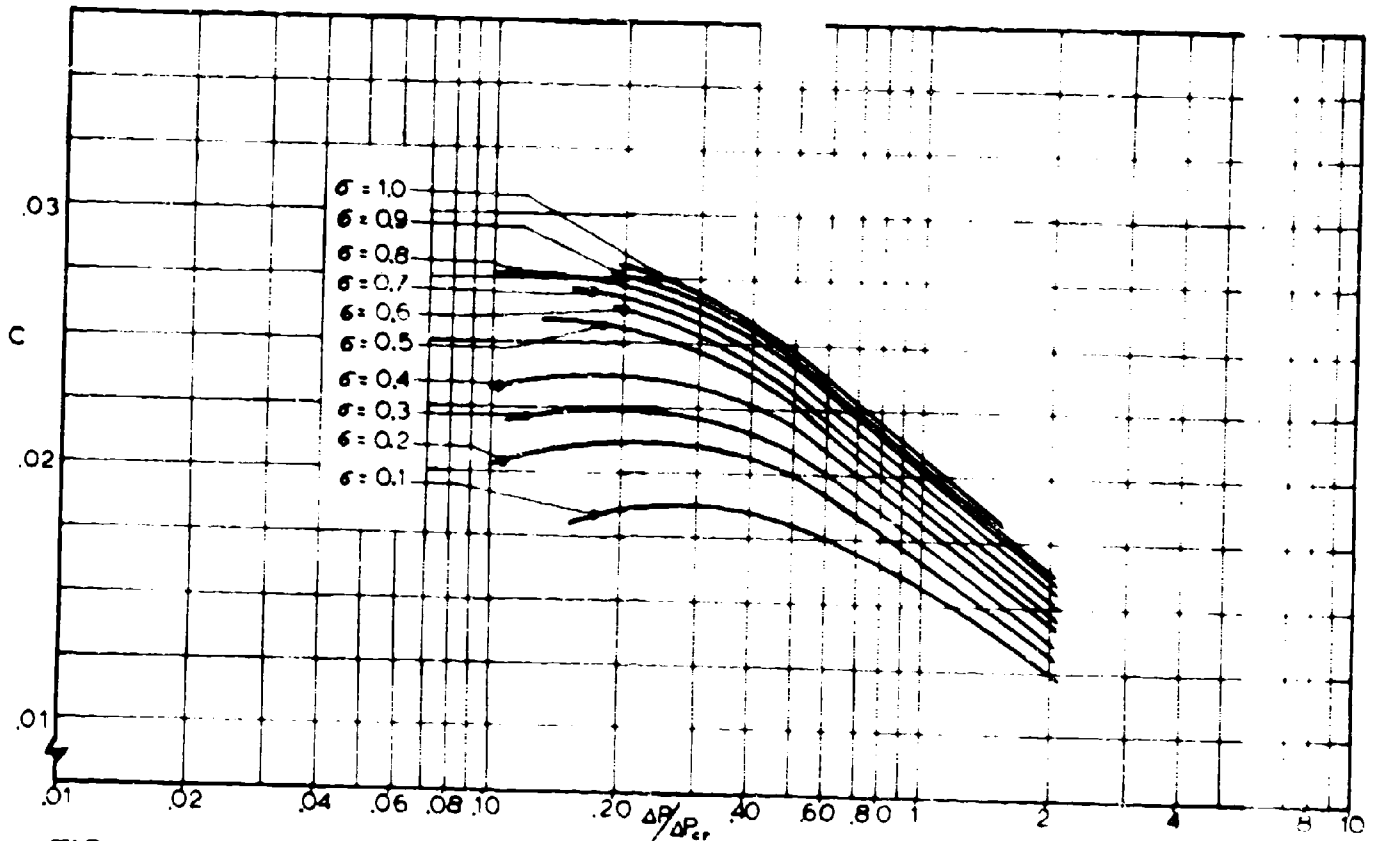


FIG 13-5. EFFECTIVE POROSITY VERSUS PRESSURE RATIO  
MIL-C-8021A, TYPE II, 300 LB/IN





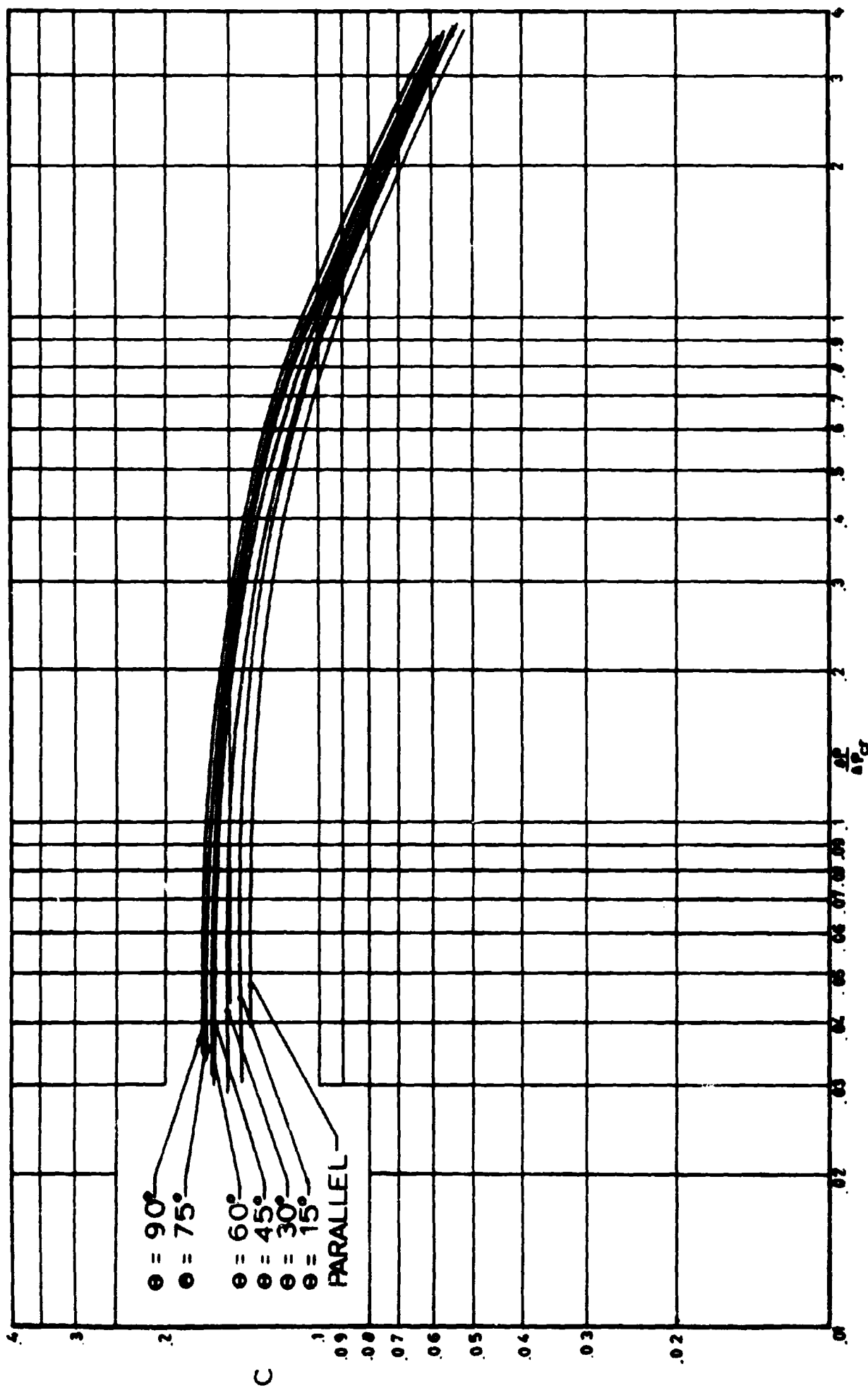


FIG 13-8. EFFECTIVE POROSITY OF STEEL RIBBON GRID CONFIGURATIONS AS A FUNCTION OF DIFFERENTIAL PRESSURE

## Project No 14

### 10.0      Study of Flow Patterns of Aerodynamic Declerators by Means of the Surface Wave Analogy

#### 10.1      Introduction

Progress Report No 19 reported the completion of the final assembly and sealing of the water channel, the assembly and initial testing of a shadowgraph and Schlieren system, and the development of a simple experimental technique for obtaining the water depth profile around the models.

#### 10.2      Present Work

##### 10.2.1    Levelling and Final Alignment

The two hydraulic jacks used to obtain a longitudinal slope of the channel were adjusted until the glass channel floor was horizontal. This was checked by ensuring the uniformity of the placid water depth throughout the channel using the micrometer depth gage as indicated in Progress Report No 19. Two gunners' quadrants obtained from government surplus were mounted on the table near the hydraulic jack supports and adjusted to zero when the channel floor was horizontal. In order to set the channel to any desired slope to correspond to the desired Froude number (simulating the Mach number), it is now only necessary to set the two quadrants to the desired elevation and operate the hydraulic jacks until the level gages of the quadrants are centered.

Next, the carriage guide rails were realigned to be parallel to the glass surface. This was done by means of an Ames dial gage mounted on the triangular stand of the micrometer depth gage. The guide rails were adjusted to be parallel to the glass surface near the corresponding side of the table to within +0.001 inch.

Finally the transverse beam of the carriage was checked for parallelism with the glass surface and adjusted by means of shims to be within  $\pm 0.005$  inch.

#### 10.2.2 Nozzle Plate Stiffening

It was observed that the 52 inch wide,  $1/4$  inch thick aluminum alloy nozzle plate tended to sag near the middle. In addition, it tended to vibrate, producing pulsations in the water flow. These undesirable effects were greatly reduced by stiffening the nozzle plate using two 4 inch by  $1\ 1/8$  inch aluminum alloy angle sections bolted to the nozzle plate along the centerline and perpendicular to it near the discharge end.

#### 10.2.3 Instrumentation

##### 10.2.3.1 Shadowgraph System

The design of the shadowgraph system was finalized and is shown diagrammatically in Fig 14-1. The light source unit consists of a 150 watt slide projector lamp with attached reflector, a condensing lens system, and an iris diaphragm; these components are mounted inside a rectangular housing located under the glass floor of the test section. Cooling air for the lamp is circulated by a 3 inch motor driven fan inside the housing. The light beam passes through the iris diaphragm and is reflected vertically upwards by a  $45^\circ$  first surface mirror. A 14 inch diameter, 14 inch focal length Fresnel lens located directly under the test section is used to produce a parallel beam of light through the test section. The shadowgraph image is formed on a frosted glass screen mounted horizontally above the model, on a frame attached to the model carriage.

This image can be viewed directly or photographed by still or movie cameras.

##### 10.2.3.2 Schlieren System

The design of the Schlieren system was integrated with

that of the shadowgraph to enable a quick change over from one system to the other. As shown diagrammatically in Fig 14-1, the Schlieren system shares the same light source, 45° mirror and Fresnel lens located underneath the channel test section, but the horizontal viewing screen directly above the model is removed and an optical assembly consisting of another Fresnel lens identical to the first one, a rotating and adjustable knife edge assembly, lens, and turning prism are mounted in its place. The parallel light beam through the test section is condensed by the second Fresnel lens and impinges on the knife edge, is turned 90° by the prism and is then projected onto a frosted glass screen mounted vertically in a frame attached to the carriage. Figure 14-2 is a photograph of the general arrangement of the upper assembly of the Schlieren system, and shows the Schlieren image of a diamond airfoil projected on the viewing screen. Figures 14-3 through 14-5 show various components of the shadowgraph and Schlieren systems; Fig 14-3 is a close-up of the 45° mirror, Fig 14-4 shows the top unit of the Schlieren system, and Fig 14-5 is a close-up of the knife edge and prism assembly. This is designed in such a way that the knife edge can be adjusted fore and aft or rotated to any angle with respect to the direction of flow. It is also possible to remove the straight edge and substitute an iris diaphragm and use this as a circular knife edge.

#### 10.2.3.3 Water Depth Probes

Two pointed probes attached to standard 1 inch travel Ames dial gages were designed for mounting on the traversing carriages as shown in Fig 14-2. Preliminary depth measurements with these probes indicate good repeatability.

#### 10.2.3.4 Water Pressure Probes

Preliminary tests with a water pressure probe consisting essentially of an impact or pitot tube connected to a micromanometer

or an inclined tube manometer showed the necessity for a careful choice of the probe dimensions. In view of the limited water depth and the desire to obtain a good resolution from the total pressure probe, it is necessary to use the minimum size of head consistent with accuracy and repeatability. Different sizes of special thin wall brass tubing have been procured and tests to determine suitable probe configurations will be conducted.

#### 10.2.3.5 Water Depth Profile Around Models

Further tests with the Eosin dye technique mentioned in the last progress report were conducted using two slightly different experimental procedures. In the first, the dye painted model was lowered vertically in position into the flowing water until it made contact with the glass floor. In the second, the model was set up in the test section prior to starting the flow circulation. In both cases, with the Eosin Alcohol concentrations used, the dye was quickly washed away from the immersed portions of the model and a sharp water line obtained. Care was taken to use short test durations of the order of four or five seconds and to watch for any pulsations of the water flow since the water line obtained represented the maximum rather than the time average water depth at that point. Further experiments may indicate the desirability of reducing the solubility of the dye to give a more representative water depth distribution.

Another dye technique with the object of indicating the range of variation of water depth at every point during the test was tried. This method uses coloring agents which form a very thin colored film which floats on the water surface and adheres to solid surfaces partly immersed in it. However, tests showed that the dye marked the stagnation point only, and separated from the rest of the boundary surface and was quickly washed away downstream.

#### 10.2.4     Models

##### 10.2.4.1   Calibration Model

The accurate calibration of the water channel involves obtaining detailed water velocity traverses along and across the test section and calibrating this with respect to the flow discharge from the pump. Such a detailed calibration can only be done after completion of the pitot probes. Meanwhile, simulated Mach numbers can be set by observing the wave angles obtained with a specified wedge profile and by checking the water depth by means of the micrometric depth probes. For purposes of initial calibration, a 10 inch long,  $9^\circ$  half angle symmetrical diamond profile was milled of solid aluminum alloy and polished as shown in Fig 7-6. This calibration model will also be used for checking the Mach number distribution in the test section prior to the complete traversing with the total pressure probes.

##### 10.2.4.2   Model of Supersonic Spiked Parachute

A model of the spiked supersonic parachute proposed in Project No 7 and based on the configuration originally given in Progress Report No 13, Fig 7-7, was designed and constructed as shown in Fig 14-6. The spike is a solid aluminum alloy wedge of  $20^\circ$  half angle, 2 inches long and  $2\frac{1}{2}$  inches high. A  $\frac{3}{8}$  inch diameter, 10 inch long threaded steel rod is screwed to the base of the wedge above the immersed section and forms the "backbone" of the model. At  $\frac{1}{2}$  inch intervals along the steel rod  $\frac{1}{8}$  inch diameter vertical holes are drilled to provide for the possible attachment of needle depth probes to determine the water depth along the centerline in the wake of the spike.

A steel fitting can be screwed into the threaded  $\frac{3}{8}$  inch diameter rod and locked at any desired distance behind the spike. It carries a transverse plexiglass plate to which can be attached by means of interchangeable bent steel rods, the curved plates representing the canopy. The main features of the model

design adopted are basic simplicity and great flexibility, enabling a quick change of the spike or canopy profile and a wide range of settings for the inlet to outlet area ratio and relative positioning of the canopy with respect to the spike. Furthermore, the model design allows for the possibility of water depth probing at practically every point of the field of interest.

### 10.3      Proposed Work

In the next reporting period, it is proposed to conduct a survey of the simulated flow Mach number in the test section by means of wave angle and water depth measurement using the diamond airfoil for calibration purposes. Simultaneously, repeatability tests with the Eosin dye technique for depth measurement will be carried out, and attempts to formulate a correction for surface tension effects will be made.

After satisfactory conclusion of these tests, simulated pressure distribution tests on the spiked supersonic parachute model at Mach 2 will be carried out. These tests will be followed by tests to optimize the design of total pressure probes, and these probes together with the micrometric depth probes already available will be used in obtaining longitudinal and transverse velocity traverses at different sections and preparing detailed calibration curves for the water channel.

Further improvements to the water channel and refinements in the experimental technique and instrumentation, such as the use of a reference grid in the test section and improvements in the flow visualization system, will be introduced when circumstances permit.



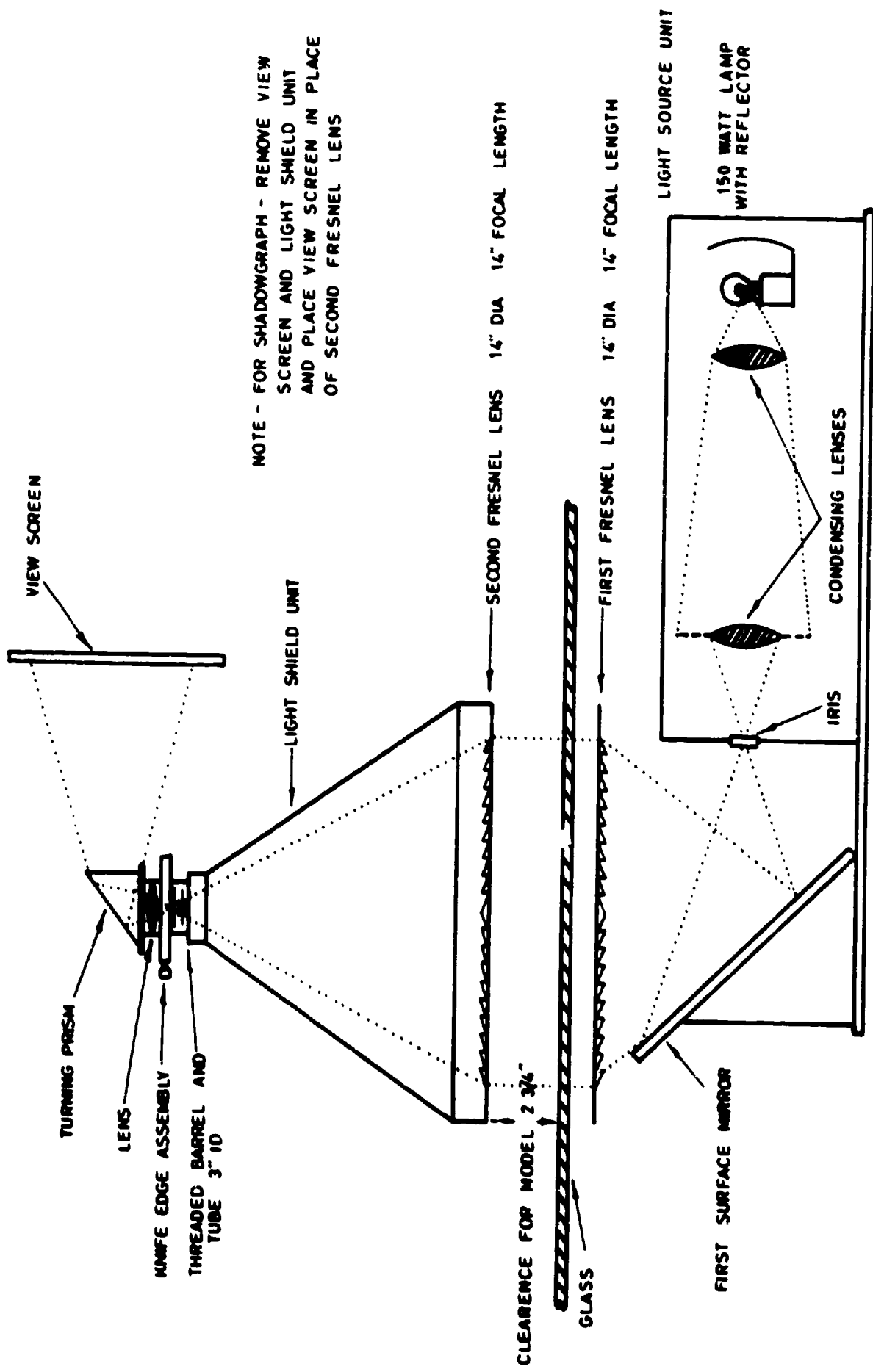


FIG 14-1. SKETCH OF SCHLIEREN AND SHADOWGRAPH



FIG 14-2. GENERAL VIEW OF UPPER COMPONENTS OF THE SCHLIEREN SYSTEM

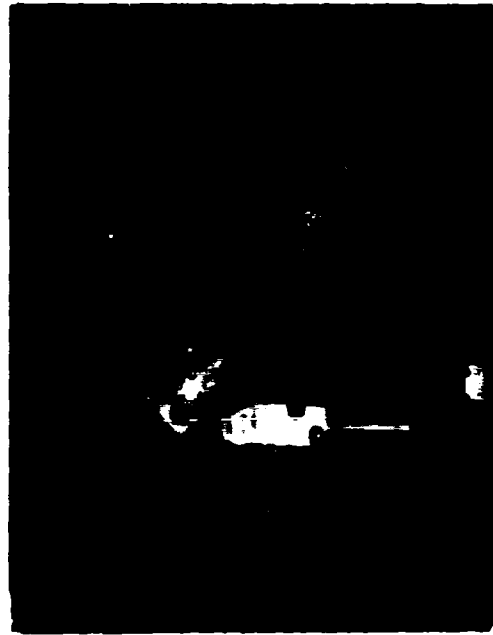


FIG 14-3. 45° MIRROR USED FOR SHADOWGRAPH AND SCHLIEREN SYSTEMS.

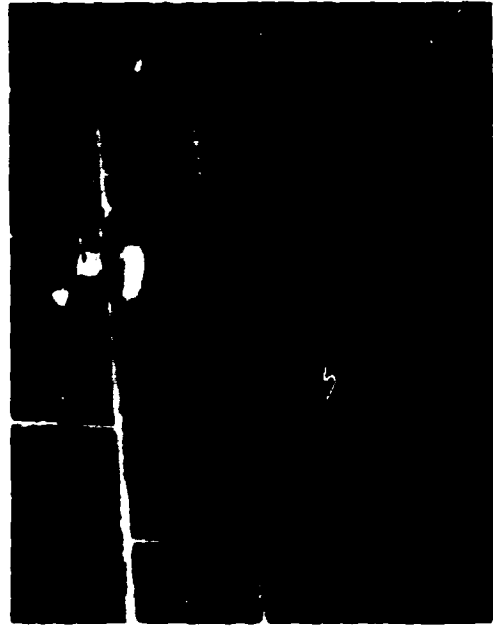


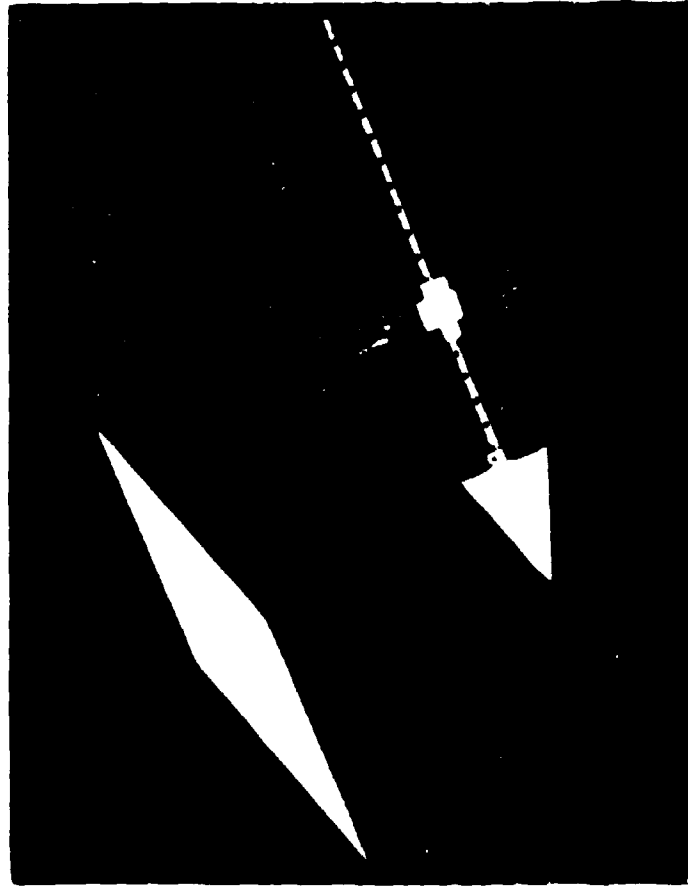
FIG 14-4. UPPER OPTICAL ASSEMBLY OF SCHLIEREN SYSTEM.



FIG 14-5. CLOSE-UP OF KNIFE EDGE ASSEMBLY AND PRISM FOR SCHLIEREN SYSTEM.



FIG 14-6. MODELS OF SPIKED SUPERSONIC PARACHUTE AND DIAMOND AIRFOIL



## Project No 16

### 11.0 Stress Analysis of the T-10 Troop Parachute

Progress Report No 18 presented an analytical method for obtaining the stress distribution over a fully inflated canopy in steady descent. The method was applied specifically to the T-10 extended skirt troop parachute, but was general enough so that it could be applied to other types of parachutes with only minor modifications.

Three minor errors have been detected in the method presented in Progress Report No 18. In the definition of terms, the modulus of elasticity,  $E$ , was defined dimensionally as  $\text{lb/ft}^2$ . This should be  $\text{lb/ft}$ . Secondly, Fig 16-8 presented a tabulation sheet for finding values of the bulge radius by use of Eqn (16.15a). The equation was incorrectly given on this tabulation sheet, and a corrected tabulation sheet is presented here in Fig 16-1. Also, in Fig 16-10 of Progress Report No 18, the decimal points in the ordinate axis for  $r^*$  were left out. This should be corrected so that  $r^*$  ranges from 0 to 0.40.

Efforts are being made to refine the above analytical method for finding stress on a fully inflated canopy. Some simplifications in the use of the theory for finding actual numerical values of stress appear to be possible, but these are not fully developed; these simplifications will be presented in future progress reports. Also, efforts are being made to extend the theory to the more complex case of finding the stress over an opening canopy. These efforts will be continued during the next period.



## APPENDIX

The authors of this report who are listed on the front page wish to acknowledge the accomplishments and assistance of the following personnel:

### Clerical Staff:

E. Zembergs, Sr. Engineering Assistant  
Beverly M. Broers, Secretary

### Graduate Students:

R. O. Bailey, Research Assistant  
D. J. Eckstrom, Research Assistant  
S. R. Hess, Research Assistant  
E. M. Linhart, Research Assistant  
D. J. Monson, Research Assistant  
L. W. Rust, Research Fellow

### Undergraduate Students:

R. E. Albrecht, Engineering Assistant  
J. Baker, Engineering Assistant  
J. W. Bushard, Engineering Assistant  
J. M. Carlson, Engineering Assistant  
D. F. Coleman, Engineering Assistant  
D. D. Evenson, Engineering Assistant  
R. W. Friestad, Engineering Assistant  
K. J. Goar, Engineering Assistant  
L. R. Jamison, Engineering Assistant  
J. M. Johnson, Engineering Assistant  
H. R. Kokal, Engineering Assistant  
H. M. Lipka, Engineering Assistant  
D. A. MacLean, Engineering Assistant  
D. E. McGee, Engineering Assistant  
W. R. Mueller, Engineering Assistant  
T. C. Nietz, Engineering Assistant  
E. H. Nierengarten, Engineering Assistant  
D. R. Nordwall, Engineering Assistant  
D. Pekarek, Engineering Assistant  
R. O. Strom, Engineering Assistant  
L. M. Timmons, Engineering Assistant  
B. J. Williams, Engineering Assistant

### Machine Shop Personnel:

J. Taube, Laboratory Machinist  
P. A. Huehnert, Wind Tunnel Mechanic